Computational reconstruction of the physical eye using a new gradient index of refraction model

Zack Dube

Thesis submitted to the Faculty of Graduate and Postdoctoral Studies in partial fulfillment of the requirements for a Master's degree in Physics

Department of Physics

Faculty of Science

University of Ottawa

Abstract

This thesis proposes and tests an individually customizable model of the human crystalline lens. This model will be crucial in developing both research on the human eye and driving diagnostic tools to help plan and treat optical issues, such as those requiring refractive surgery.

This thesis attempts to meet two goals: first, it will determine whether this new lens model can reproduce the major aberrations of real human eyes using a computational framework. Second, it will use clinical information to measure how well this model is able to predict post-operation results in refractive surgery, attempting to meet clinical standards of error.

The model of the crystalline lens proposed within this thesis is shown to be valid, as it is able to both reproduce individual patient's optical information, and correctly predicts the optical results of a refractive surgery of an individual human eye within clinical standards of error.

Contents

List of Figures

List of Tables

1 Introduction

1.1 Goal of the project

The goal of this project is to computationally construct and test a model of the human crystalline lens from anatomical and optical data. This model is designed to be customizable to reproduce the particular optical properties of an individual human eye. The validation of this model is the next step in achieving the ambition of individualized health care. The computer software developed in this thesis could become the basis for diagnosis and treatment planning for patients with optical problems in the future.

1.2 Working Hypothesis and Research Approach

This project aims to computationally construct an eye model that can reproduce the optical properties of an individual human eye using a new crystalline lens model for customization. Such a model must be able to use anatomically correct features, including corneal and lenticular surface information, as well as a lenticular gradient index of refraction (GRIN).

The principal hypothesis is that a customizable model of the crystalline lens can be constructed which will be able to predict the optical parameters of an individual human eye. This model must be constructed using only aberration information obtainable from common clinical aberrometer readings and biometry information available in-vivo. This study does not have access to a set of full biometric information, and attempts to use only corneal data with no knowledge of the crystalline lens or eye length. Even with this limitation, the model proposed in this work will be shown to be valid in this thesis.

A two step approach will be taken to test this hypothesis. First, we will determine whether this new lens model can reproduce the major aberrations of real human eyes using a computational framework. In a second test, we will use clinical information to measure how well this model is able to predict post-operation results in refractive surgery. To achieve this, the following steps were taken:

- Develop a computational infrastructure for ray tracing, including through gradient index profiles such as the lens.
- Perform wavefront analysis of the ray trace to obtain aberration information of the computed model.
- Import clinical aberration and corneal topography of pre-surgery patients
- Implement a minimization algorithm to vary any free biometric or physical parameters in order to reconcile error in defocus and spherical aberration between clinical and computational information. This yields a version of the patient's lens.
- Use the fitted lens to validate post-surgical results. If correct, our lens model has succeeded.

The clinical information used in this text is supplied by the Ottawa Hospital Research Institute (OHRI). All participants signed consent forms approved by the OHRI Research Ethics Board. No personal identifiers were used in any of the analysis.

1.3 Thesis Structure

The remainder of Chapter 1 is dedicated to presenting basic information about the human eye, both optically and physically. It will also list documented ranges of

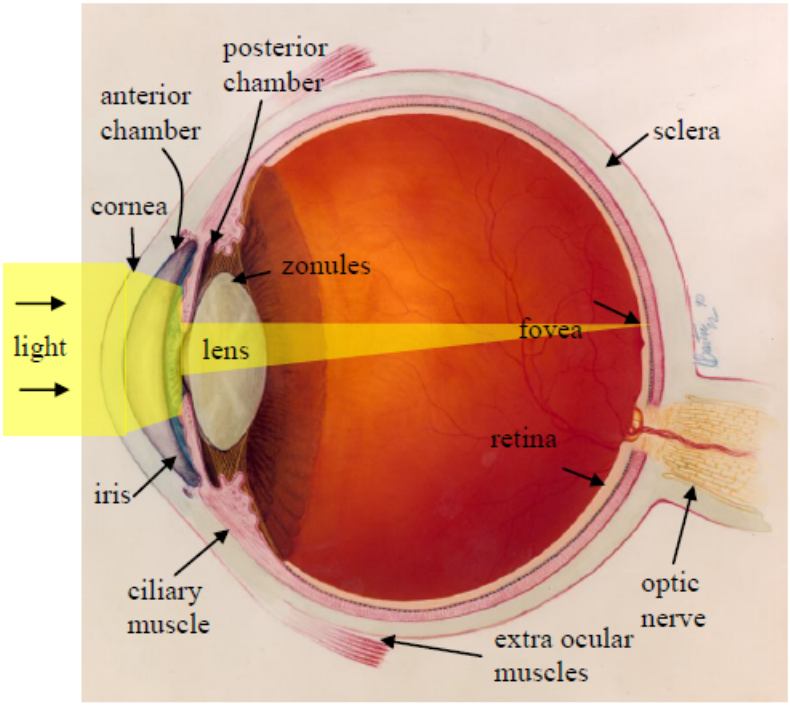

Figure 1.1: An schematic diagram of the human eye. Image courtesy of the National Eye Institute, National Institutes of Health (www.nei.neh.gov)

human eye parameters. Chapter 2 discusses the historical background of modelling the crystalline lens and gives an overview of the model proposed in this project. Chapter 3 presents the computational techniques used to study the proposed model. In Chapter 4, the research methodology is shown, and the results of the computational study are analysed. Chapter 5 presents a discussion of these results and shows their validity. Potential future work will also be covered in Chapter 5, and conclusions given.

1.4 Anatomy of the human eye and crystalline lens

Human vision is due to the coordination of two separate anatomical entities: a physical system of internal optics, and the neural system dedicated to processing light

signals. The work presented in this thesis is limited only to the physical optics of the eye, and the processing elements will not be discussed.

Figure 1.1 shows the anatomy of the human eye. Light is first refracted as it enters the cornea, a collagenous structure transparent to the entire wavelength range of human vision (380 - 780 nm) [1, 2]. Behind the cornea is the anterior chamber, filled with aqueous humour. The aqueous humour consists of mostly water, but also contains proteins and ions. Next is the iris, which acts as an aperture for the eye. It is controlled by the nervous system and adjusts in size to allow more light into the eye when conditions are dark, or vice-versa, to restrict the amount of light entering the eye under bright conditions. Behind the pupil is the crystalline lens (referred to as the lens for the remainder of this document), contained in the posterior chamber. The lens is a flexible cellular structure consisting mostly of water and proteins, and is attached at its equator to the ciliary muscles by elastic fibres called zonules. The rest of the posterior chamber is filled with vitreous humour, another mixture of water, proteins and nutrients.

At the back of the eye is the retina, a layered structure of nerve cells, containing photoreceptors called rods and cones that transform the physical stimulus of light into a neural signal. Rod cells are more sensitive to lower light conditions, whereas cones function better at higher light levels. At the centre of the field of vision is the fovea, the area of highest visual resolution.

In order to adapt to varying visual distances, the eye undergoes a process called accommodation, shown in Figure 1.2, in order to change its refractive power. During accommodation, the ciliary muscles expand and contract in order to change the shape of the lens. When the muscles are relaxed the zonules are tense, causing the lens to flatten. This is the unaccommodated state and is more appropriate for distant vision. In order to focus on objects closer to the eye, the ciliary muscles contract, releasing

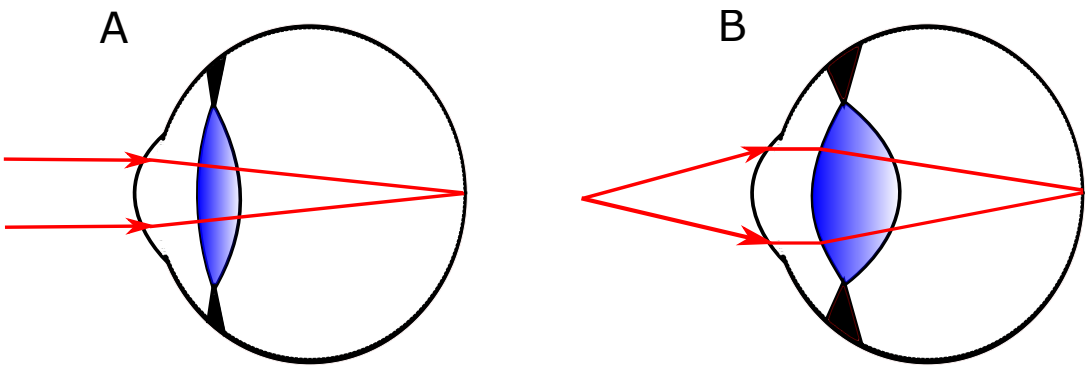

Figure 1.2: Eye A shows the lens in an unaccommodated state: rays from infinity are focused onto the retina. Eye B shows an accommodated lens: a nearby object is imaged on the retina.

the tension of the zonules on the lens. This causes the lens to increase in thickness. As an individual ages, the lens becomes denser, and the process of accommodation will eventually become impossible, fixing the eye in its relaxed state. This is known as presbyopia, and will affect almost everyone over 50 years of age.

1.5 Optical properties of the eye and lens

An average unaccommodated eye has a total refractive power of approximately 60 D (where D = $\frac{1}{m}$), corresponding to a focal length of 22 mm in water (focal length is defined as index of refraction divided by dioptric power). This power is due to the contribution of the cornea, which makes up approximately 66% of the refractive power, and the lens, which contributes the remaining 33% of the refractive power. Refraction occurs at both surfaces of the cornea (48 D to the anterior and - 6 D to the posterior respectively), and both surfaces of the lens. The lens is distinct optically from the cornea because it has a gradient index of refraction, so refraction also occurs constantly as light traverses the lens. The iris acts as an aperture for the system, and

an average adult eye has a length of about 24 mm. [1, 2]

The cornea is about 0.6 mm thick, with a uniform refractive index of 1.376. The anterior and posterior surfaces are usually modelled as conic sections (ellipses) with average values of apical radii of curvatures of 7.77 and 6.40 mm and asphericity (conical constant q) of -0.18 and -0.60 respectively. [2]

In its unaccommodated state, the lens has an average thickness of about 4 mm, with a refractive power of approximately 19 D. The diameter of the equatorial plane of the lens is 9 mm. Again, the surfaces are usually modelled as conic sections, with average anterior and posterior radii of curvature of 12.40 mm and -8.10, and asphericities of -0.94 and 0.96 respectively. During accommodation the lens thickness increases by 0.3 mm and moves towards the cornea, and the radii of curvature of both surfaces decreases drastically. Due to these changes, the refractive power of the lens can increase by about 50% in a young eye. [1]

The gradient index of refraction of the lens, GRIN, will be discussed in more detail later in this thesis. A brief summary will also be presented here. The index of refraction is lowest at the lens surface, and increases until the centre of the lens, from about 1.386 at the surface to 1.406 in the nucleus. In order to recreate the equivalent power with a homogeneous lens, a refractive index of 1.42 (higher than anywhere found in the eye) would be required. [2]

Like any optical component, the cornea and lens are not ideal, and as such introduce optical aberration to human vision. In this thesis, only monochromatic aberrations will be considered, but it is worth noting that chromatic aberrations also exist in the eye. Monochromatic aberrations will be discussed again in more detail in Chapter 2, but a brief overview will be presented here.

The most common aberration in the eye is defocus. In humans the typical range is about $\pm 10D$ (about 18% of the eye's power), though extreme cases can show much

more. Defocus is generally easily fixed with glasses or contact lenses.

Also important in the human eye is spherical aberration (SA). This occurs when paraxial rays have a different focal length than marginal rays for on axis points. SA is exhibited by both the cornea and the lens; the cornea contributes a larger positive value, while the lens contributes a smaller negative value, compensating for some of the corneal SA. The negative value of the spherical aberration of the lens is due to the GRIN. Anatomically, there are a number of other reasons why spherical aberration vary, which have been studied extensively in several papers. [3–5] As a brief summary, the following trends are shown in these papers. Accommodation has been shown to have a significant effect on SA: when the eye is relaxed, the spherical aberration is more positive, while when accommodating, the spherical aberration decreases due to the change in asphericity in the lens surfaces. Similarly, due to the change in shape of the lens as a person ages, the spherical aberration will decrease over their lifetime.

A list of physical ranges for human eye parameters is presented in Table 1.1, with results listed from many studies. [3, 5–34] It is clear from this table that each human eye is quite distinct, which is the driving force behind our research. An eye model which assumes average values cannot reproduce the individual optical properties of individual eyes.

Eye Component	Physical Range
Axial Length	23.3 - 24.9 mm
Cornea Centre Thickness	0.51 - 0.58 mm
Lens Thickness	4.2 - 4.3 mm
Cornea Anterior Curvature	7.70 - 7.98 mm
Cornea Posterior Curvature	6.36 - 6.70 mm
Cornea Anterior Asphericity	-0.72 - 0.0
Cornea Posterior Asphericity	-1.00 to -0.4
Lens Diameter	6.20 - 9.85 mm
Lens Anterior Radius	4 - 25 mm
Lens Posterior Radius	-3 to -12 mm
Lens Anterior Asphericity	-6.06 - 3.27
Lens Posterior Asphericity	-1.19 - 1.09
Lens Central Index	1.39 - 1.41
Lens Surface Index	1.36 - 1.41
Lens Power	15 - 44 D
Lens Focal Length	16 - 75 mm
Lens Spherical Aberration	-0.3 - 0.6 μm
Lens Astigmatism	-1.25 - 0.3 μm
Lens W factor*	2 - 10

Table 1.1: Physical ranges of parameters in the human eye, gathered across a large body of work. [3, 5–34] * The W factor is the key parameter suggested by this model, and will be discussed in more detail in Chapter 2. It has not been tested on humans yet, so animal results are listed.

2 Background

This chapter will delve into the background of crystalline lenses. It is fairly straightforward to measure most physical parameters of the eye to create customizable eye models, but what is missing is the ability to obtain a satisfactory description of the lens, specifically its gradient index of refraction (GRIN). The critical advancement in our model is the ability to individually customize the GRIN.

2.1 Historical Crystalline Lens Models

The first models of the crystalline lens used a single homogeneous lens to describe the refractive index profile, along with spherical (or aspherical) surfaces. While homogeneous index models such as the Gullstrand-Legrand [35] or Indiana [36] eye models offer rough approximations of the eye's optical properties, they cannot accurately model higher order aberrations (such as spherical aberration), giving clear evidence that the lens GRIN needs to be taken into account.

One of the first attempts to characterize a non uniform GRIN was by Nakao in 1968 [37] (rabbit) and 1969 [38] (monkey and human). To approximate a true gradient, isoindicial shells were defined in the anterior and posterior lobes with different eccentricites. There were several variations of the model constructed with both varying central index and rate of index increase, which were used for ray tracing. Unfortunately, these were never compared to real data and were later shown to be inaccurate.

Pomerantzeff (1972) [39] developed a model for the crystalline lens with an "onion-like" structure, with a nucleus surrounded by about 100 layers (finding that a variation of the number of layers by about 20% caused little change). The gradient index of refraction of these layers is represented by a third order function, ranging from 0 to

1, where the value at 0 gives the surface index and the value at 1 gives the core index. Unfortunately, this model did not have access to sufficient physical information from real human eyes, and as such was later shown to be unsuccessful, but was later improved by Pomerantzeff in 1984. This time, the model had 200 layers and used a more accurate lens thickness and curvature. The new model had a varying index parameter, though they were unable to definitively decide which matched experimental results best.

An important step for GRIN analysis was completed by Chu in 1977 [40] when he determined a non-destructive method to calculate an index profile of optical fibre. By measuring the height of input rays and the exit angle of the output rays, he showed it was possible to analytically recover the GRIN of a spherically symmetric medium. This remains true if the fibre is clad. This would prove to be an invaluable tool, used many times (for example by Campbell et al. in 1981 and 1984 to study rat lenses [41, 42] and Munger in 1990 to study human lenses [43]).

Jagger (1990) [44] developed individual models of the cat crystalline lens based on measurements of the refractive index of frozen sections in the sagittal plane of cats' left eyes. Isoindicial curves were generated that followed a different curvature in the anterior and posterior halves, but were joined smoothly at the lens centre. In order to test this model, the right eyes of the cats were subjected to laser ray tracing ex-vivo and compared to theoretical ray tracing of the left. Good agreement was found for the paraxial focal length and spherical aberration.

Smith, Pierscionek and Atchison (1991) [45] were the first to combine both aspherical surfaces and a GRIN lens. They considered four different lens shapes and distributions. The first has elliptical isoindicial contours that have equal anterior and posterior curvatures. The second is similar, except that the anterior and posterior contours now have different curvatures. The third model expands on the second by

allowing the contours to vary in shape from the lens surface. Finally, the fourth model allows asphericities to be negative for the shape of the contours, and does not smoothly connect the contours of the anterior and posterior lobe at the equator. They conclude that none of these models will exactly match the lens mathematically, but that the fourth comes the closest to physical measurements.

Al-Ahdali [46] created another shell model of the lens in 1995 which uses a laminated structure. This model is influenced by Pomerantzeff's earlier model, this time taking 600 layers, although it does not require a homogeneous lens core. Each lamina is 5.6 μm thick, with an index of refraction increasing exponentially from the core to the surface. The model may be reduced to three key parameters: one which controls the increment between two successive surfaces, a second which controls the curvature gradient of individual shells, and finally the parameter that controls the variation of the index from the core to the surface. These parameters were then varied to attempt to best match physical measurements of the average human eye, and full agreement was found.

In 1997, Liou and Brennan [11] published a GRIN model that is considered to be very successful in reproducing average optical properties of human eyes. First, they use a large sample size of biometric information to characterize every surface in the eye. Their GRIN model separates the lens into anterior and posterior regions, where the GRIN is:

$$n(w, z) = n_{00} + n_{01}z + n_{02}z^2 + n_{10}w^2 \tag{2.1}$$

In this case, w is the radial component, and z is along the optical axis, with $z = 0$ at the centre of the lens. The coefficients they use are listed in Table 2.1.

This model successfully predicts both spherical and chromatic aberration within

Coefficient	Anterior Value	Posterior Value
n_{00}	1.368	1.407
n_{01}	0.049057	0.00000
n_{02}	-0.015427	-0.006605
n_{10}	-0.001978	-0.001978

Table 2.1: Values of coefficients used in Liou and Brennan's GRIN model

empirical results.

Huang (2006) [47] improved upon the Liou-Brennan schematic eye by using additional terms to represent the GRIN in one single equation rather than considering anterior and posterior lobes separately:

$$\begin{aligned} n(w,z) = n_{00} + n_{01}z + n_{02}z^2 + n_{03}z^3 + n_{04}z^4 + n_{05}z^5 + n_{07}z^7 \\ + n_{10}w^2 + n_{20}w^4 + n_{12}z^2r^2 + n_{01'}z^{2/3} + n_{02'}z^{2/5} \end{aligned} \tag{2.2}$$

In this equation, there are three different explanations for terms. Firstly, the constant, z^2, r^2, z^4, r^4, and z^2r^2 terms model the ellipsoidal shape of the isoindicial surfaces and the symmetrical distribution of GRIN along the transverse plane. Next, the z, z^3, z^5 and z^7 terms describe the asymmetrical distribution along the optical axis where $|z| > 1$. Recall that in this model, $z = 0$ is at the centre of the lens. Finally, $z^{2/3}$ and $z^{2/5}$ are used to model the asymmetrical distribution when $|z| < 1$. Huang shows that this model is functionally nearly identical to the Liou model, but has more options to be fully customized to an individual.

Navarro (2007) [48] presents a model lens that is designed to be flexible in order to allow for individual distributions and ageing. The model is based on Smith's study [45], and uses a power function for the GRIN, allowing the surfaces to connect abruptly at the equator of the lens. The individualization of the model comes from

varying the power law of the GRIN, and while a step forward towards an individual eye model, the focal length was shown to be off by approximately 6 D.

In 2012, Bahrami and Goncharov [49] developed a new class of GRIN lens where the isoindicial contours mimic the external shape of the lens. The benefit of this type of model is that it has an invariant geometry GRIN structure, meaning that it allows analytical paraxial ray tracing. They present the solution based on initial ray conditions, and go on to show that it provides a reasonable optical power. However, the weakness with this model is that only works with paraxial rays, and marginal rays are required to be able to model higher order aberration.

2.2 Our Eye Model

Given the history of the characterization of the crystalline lens, it is clear that a new model is necessary for truly successful individualized eye models. Such a model is presented in this section: a model that has GRIN parameters designed to replicate individual behaviour.

Here, the model that is presented in this thesis will be discussed, initially defined by R. Munger and C. Wilson [34]. As discussed in the previous section, the surface of the cornea and crystalline lens may be represented sagitally as an aspheric conic surface. Mathematically, this is given as:

$$f(x,y) = \frac{(x^2+y^2)c}{1+\sqrt{1-(x^2+y^2)c^2(1+q)}}$$

Here, the sag (defined as z-distance from the apex of the surface) is given by the radial distance from the centre of the lens. The factor c is the apical curvature of the lens (the inverse of radius of curvature) and q represents the asphericity of the conic. $q = 0$ for a sphere, $q = -1$ for a parabola, $-1 < q < 0$ for a prolate ellipse and $q > 0$

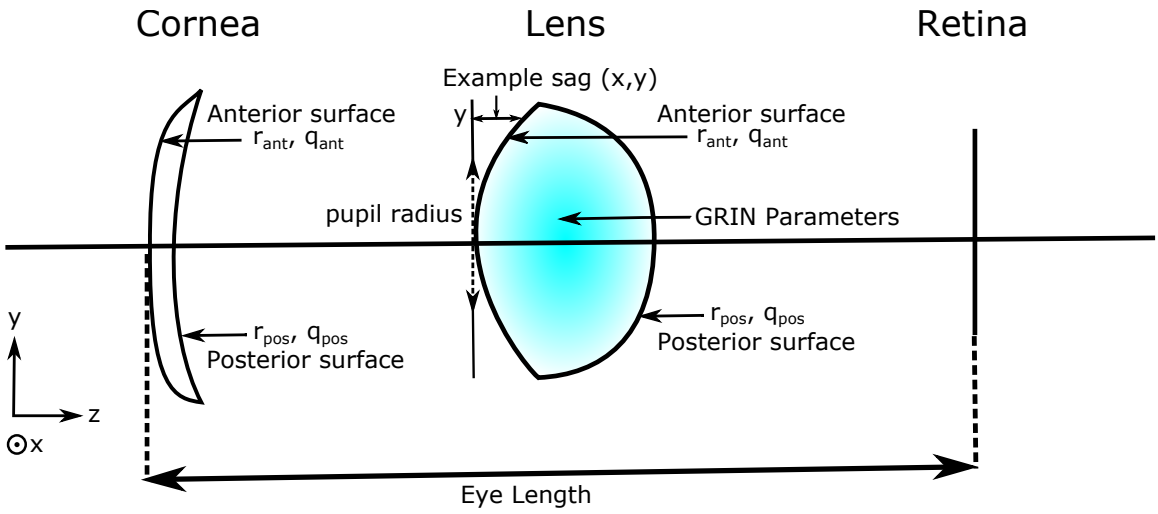

Figure 2.1: The surfaces of the two optical elements of the eye, the cornea and the retina. To be described with conic sections, each needs both a radius of curvature and ellipticity. In addition to the surface information, the other parameters needed for this thesis are GRIN related, and the pupil radius and eye length. The coordinate system is designed such that the axis of propagation is the z-axis (or the optical axis), the x-axis is horizontal, and the y-axis is vertical. The origin is at the center of the lens (on the optical axis, in the equatorial plane.)

for an oblate ellipse. A schematic of the eye introducing this coordinate system and the discussed surfaces are presented in Figure 2.1.

The equatorial GRIN is rotationally symmetric with a parabolic index profile, and is described by equations 2.3 to 2.6. We know that the equatorial plane ($z = 0$) has a parabolically scaled GRIN [34], which is described exactly by equations 2.3 to 2.5. For $z \neq 0$, the equatorial gradient is rescaled using equation 2.6.

$$n(r,z) = n_c\sqrt{1 - \frac{n_c^2 - n_s^2}{n_c^2}p(r,z)} \tag{2.3}$$

$$p(r,z) = C_0 + C_1K(r,z)^2 + C_2K(r,z)^4 \tag{2.4}$$

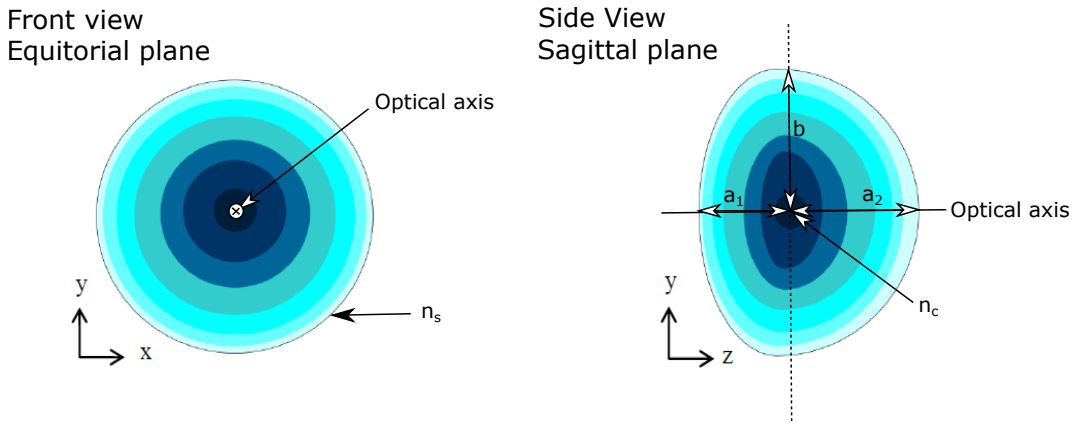

Figure 2.2: A front and side view of the lens, showing GRIN parameters a_1,a_2, and b, as well as central and surface indices. The coordinate system is also shown.

$$k(r,z) = \left(\frac{r}{b}\right)^2 + \left(\frac{z}{a}\right)^2 \tag{2.5}$$

$$K(r,z) = \sqrt{\left(\frac{r}{b}\right)^2 + \left(\frac{z}{[1-\sqrt{(k(r,z)}]^W (b-a)+a}\right)} \tag{2.6}$$

Shown in Figure 2.2, $r(=\sqrt{x^2+y^2})$ is the radial distance from the optical axis, b is the equatorial lens radius, n_c and n_s are the indices of refraction of the lens at the centre and surface respectively, and C_0,C_1,C_2 are constant parameters which scale the GRIN parabolically from n_c to n_s in the equatorial plane. a is the thickness of the lens along the optical axis and W, which is one of the main innovations of this model, serves to adjust the index gradient curve (to be discussed shortly). It is important to note that the anterior and posterior sections of the lens must be described uniquely with this functional form, as they have different surface shapes and thicknesses.

Consider index of refraction values along the optical axis: when at the surface, $z = a$ and $r = 0$, so $k(r,z) = 1$. When following through with $k = 1$, it is seen that $n(r,z) = n_s$, as expected. Similarly, at the centre of the lens equatorially, along the

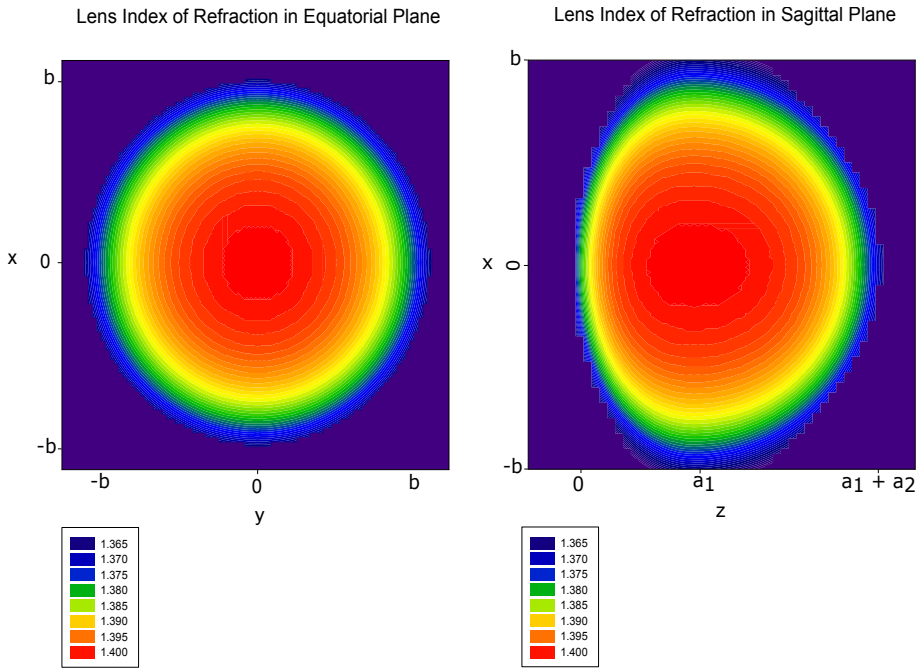

Figure 2.3: A cross sectional illustration of the index of refraction in this lens model. The index of refraction is symmetrical about the optical axis, and varies from spherical to elliptical from the exact centre to the outside surfaces in the sagittal plane. W was taken as 3.0 for this figure, with C_0, C_1 and C_2 parameters fixed as described in Chapter 2.3, and other lens parameters taken to be average.

optical axis, $z = 0$ and $r = 0$, yielding $k(r, z) = 0$. When this is the case, it is found that $n(r, z) = n_c$, again as expected. Along the equatorial plane, at $r = b$, $z = 0$, yielding $n(r, z) = n_s$. A contour plot of the index profile in the equatorial and sagittal plane is shown in Figure 2.3.

From this plot it can be seen that near the equatorial place, the GRIN has (nearly) spherical isoincidental contours, whereas at the surface, the isoincidental contours are elliptical. This behaviour corresponds to what has been seen in human lenses, which are known to have almost constant central core indices that are spherically symmetric. This change in symmetry is due to the effects of the W parameter. The

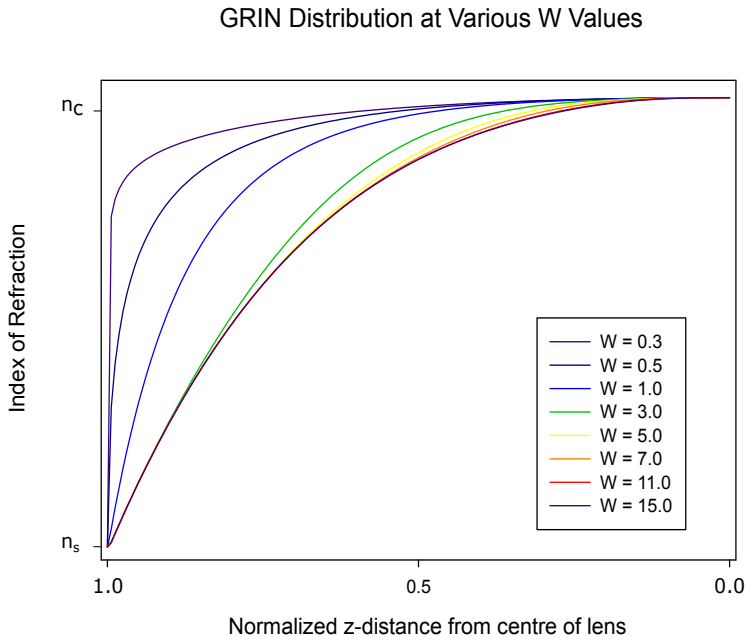

Figure 2.4: Variation of the lenticular index of refraction on the optical axis ($r = 0$) with various W factors. Average lens parameters and C_0, C_1 and C_2 parameters fixed as described in Chapter 2.3 were used.

term $[1 - \sqrt{(k(r,z)}]^W (b - a)$ acts to modify the rate at which the GRIN goes from spherical to elliptical isoincidental contours in the meridional plane. W is a very significant addition to this model, as it will vary from person to person, and is key in modelling an individual lens. Index of refraction curves for varying W values are demonstrated in Figure 2.4.

2.3 Reducing Parameter Space

The eye model proposed in this thesis takes an already complex system and adds many new parameters. It would be highly demanding computationally if all parameters had to be optimized. Instead, we will draw upon relationships that may be formed between biometric and optical properties in the eye in order to simplify the model

significantly.

In 1999, Glasser and Campbell [19] published a study of 19 pairs of donor human eyes. Each lens was characterized using digital profiling, and the surface information as well as refractive power were found using this data. They showed statistically significant relationships between the anterior radius of curvature of the lens and many of the other biometric and optical properties. Firstly, they found that the focal length of the eye (in mm) is linearly correlated with the anterior radius of curvature (mm) with:

$$FL = 3.955 r_{ant} + 13.853 \tag{2.7}$$

If the position of the lens and overall length of the eye are known, this relationship determines a unique anterior radius of curvature that will focus light on the retina.

Secondly, Glasser and Campbell showed that the anterior radius of curvature also correlates to the posterior radius of curvature and the lens equatorial diameter linearly:

$$r_{pos} = -0.261 r_{ant} - 2.631 \tag{2.8}$$

$$b = 0.11 r_{ant} - 2.916 \tag{2.9}$$

In 2004, Manns [17] et al published a topographical study on the cornea and lens, and found that the anterior radius of curvature additionally defines the anterior asphericity, with:

$$q_{ant} = 1.22 r_{ant} - 8.10 \tag{2.10}$$

When Manns similarly compared the posterior radius of curvature to the posterior asphericity, he concluded that the relationship was not statistically significant. However, all data agreed well with relationship found within a range of +/- 1.5. This

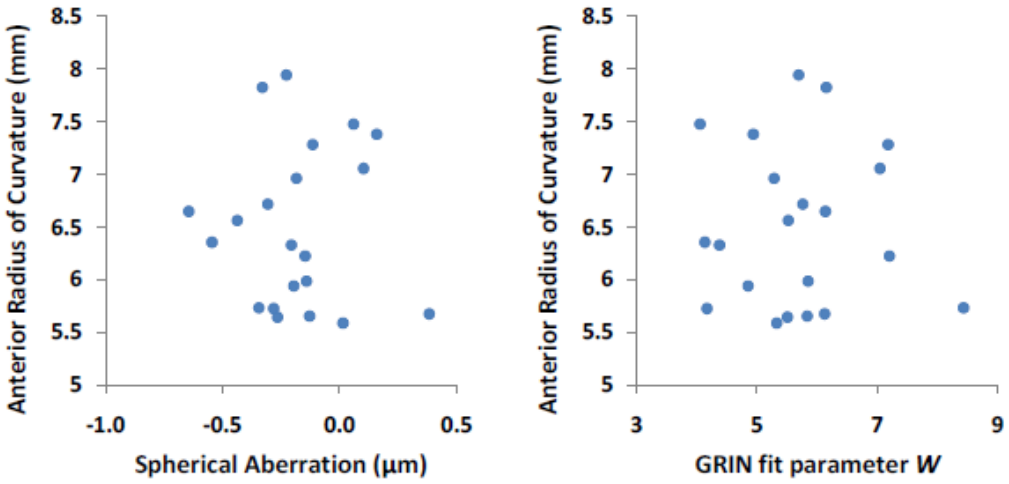

Figure 2.5: Spherical aberration and W parameter vs anterior radius of curvature over many different animal lenses. These plots show no statistical correlation.

allows to redefine the free parameter of posterior asphericity as variance of asphericity from the following relationship, providing both an initial guess and limiting range:

$$q_{pos} = 0.97 r_{pos} - 6.34 \tag{2.11}$$

In her study in 2010, Wilson [34] (Figure 2.5) also performed an analysis using a Pearson correlation coefficient table to compare relationships between parameters in the eye model used in this thesis. She found that in animal eyes, there is no correlation between lenticular anterior radius of curvature and the W parameter or spherical aberration. As expected, this parameter must be left free to model individual eyes.

Wilson further analysed lenses of many different species (pig, rabbit and cow) with the outcome showing that a single set of equatorial GRIN parameters (i.e. C_0,

C_1 and C_2) may be used across a species without effecting the reproducibility of optical properties. Using the results from an experimental ray tracing set up, Wilson performed a fit of GRIN parameters within a 95% confidence value. GRIN parameters found among many pig lenses were compared for statistical differences: a statistical p-value > 0.05 indicates no significant differences in parameters between lenses. P-values were found to be 0.542 for C_0, 0.256 for C_1 and 0.397 for C_2. This indicates that C_0, C_1 and C_2 may be considered the same across individuals in a species.

Furthermore, Wilson compared the C_0, C_1 and C_2 among cows, rabbits and pigs. The results are shown in Figure 2.6. Again, across the three species, no statistically significant differences were found (p = 0.519 for C_0, p = 0.687 for C_1 and p = 0.169 for C_2).

This evidence shows that not only can the same C_0, C_1 and C_2 values be used across a species, but that the same values are universally valid among every species tested, within statistical significance. This reduces the parameter space of our GRIN model significantly, and will be applied to our human model testing.

2.4 Wavefront theory: Zernike Polynomials

In this section, a brief theory of wave aberration as relevant to optical physics will be presented.

We look to describe the wavefront aberration as a sum of basis functions F_i: $\Omega(\rho, \theta) = \sum_{i=0}^{\infty} a_i F_i(\rho, \theta)$, where a_i is a normality coefficient. Note that for simplicity, a polar coordinate system will be used for this discussion, though there is a Cartesian analogue which could be obtained using the usual transforms. [50]

Until the 1990's, the power expansion defined by Seidel was used for describing wavefront error. This produced the accepted set of aberrations at the time, such as

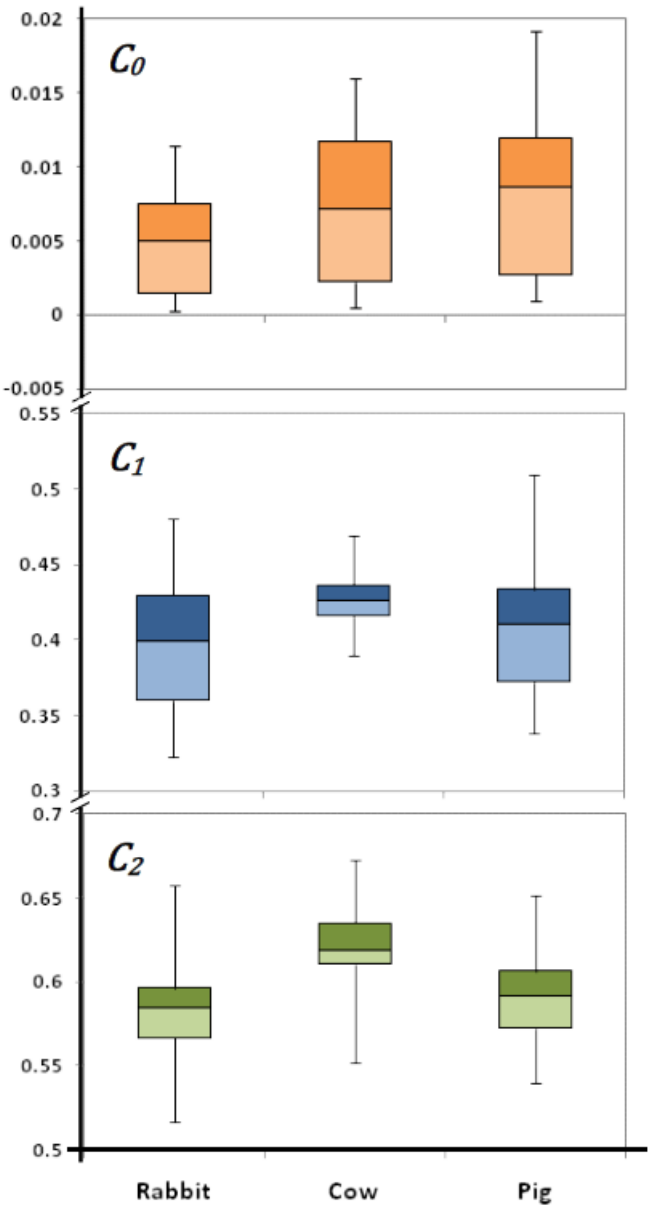

Figure 2.6: Values of C_0, C_1 and C_2 shown over three different species. The bottom error bar indicates the 5^{th} percentile, while the top error bar the 95^{th}. The bottom and top of the box are 25^{th} and 75^{th} percentiles respectively, and the middle line the mean. Figure copied with permission from Wilson [34]

distortion, field curvature, astigmatism, coma and spherical aberration. The Seidel expansion is given as:

$$S_i(\rho,\theta) = S_\alpha^\beta(\rho,\theta) = \rho^\alpha \cos^\beta \theta \tag{2.12}$$

The problem that arises with this series is that it is not orthonormal.

We require that the basis functions are orthonormal:

$$\frac{1}{\pi}\int_0^1 \int_0^{2\pi} F_i(\rho,\theta)F_j(\rho,\theta)\rho d\rho d\theta = 0 \tag{2.13}$$

when $i \neq j$, and that

$$\frac{1}{\pi}\int_0^1 \int_0^{2\pi} F_i(\rho,\theta)F_i(\rho,\theta)\rho d\rho d\theta = 1 \tag{2.14}$$

where i is the order of the term, α is the radial degree and β is the azimuthal frequency. Additionally, $\beta \leq \alpha$ and $\alpha - \beta$ being even must be satisfied.

In the case of visual optics, the Zernike polynomials are a more popular option. Unlike the Seidel series, the Zernike polynomials are orthogonal. The Zernikes also contain terms analogous to the primary Seidel aberrations, and were chosen by the Optical Society of America as a standard for discussing optical aberrations of the eye in 1999 [51]. The Zernike polynomials are mathematically described as:

$$Z_i(\rho,\theta) = R_\alpha^{|\beta|}(\rho)\Theta^\beta(\theta) \tag{2.15}$$

Again, α is the radial degree and β is the azimuthal frequency, as well as $\beta \leq \alpha$ and $\alpha - \beta$ must be even . Furthermore, $R_\alpha^{|\beta|}$ and $\Theta^\beta(\theta)$ are:

$$R_\alpha^{|\beta|}(\rho) = \sqrt{\alpha+1}\sum_{s=0}^{\alpha-|\beta|/2} \frac{(-1)^s(\alpha-s)!\rho^{\alpha-2s}}{s![(\alpha+\beta)/2-s]![(\alpha-\beta)/2-s]!} \tag{2.16}$$

$$\Theta^{\beta}(\theta) = \begin{cases} \sqrt{2}\cos|\beta|\theta & (\beta \geq 0) \\ 1 & (\beta = 0) \\ \sqrt{2}\sin|\beta|\theta & (\beta < 0) \end{cases} \tag{2.17}$$

A list of the most visually important aberrations is presented in Table 2.2, showing astigmatism, defocus, coma and spherical aberration. These polynomials are represented visually in Figure 2.7. Note that our software uses Cartesian coordinates rather than polar, so the Cartesian forms of the polynomials are listed. It is also worth noting that it is impossible to use an infinite set of polynomials, and that representing a wavefront with a truncated set always introduces some error. Our software computes the first 27 terms (up to the 6^{th} order), which is the accepted limit of our ability to measure human eyes.

Name	Polynomial
Y Astigmatism	$\sqrt{6}(2xy)$
X Astigmatism	$\sqrt{6}(x^2 - y^2)$
Defocus	$\sqrt{3}(2x^2 + 2y^2 - 1)$
X Coma	$\sqrt{8}(3x^2y + 3y^3 - 2y)$
Y Coma	$\sqrt{8}(3x^3 + 3xy^2 - 2x)$
Spherical Aberration	$\sqrt{5}(6x^4 + 12x^2y^2 + 6y^4 - 6x^2 - 6y^2 + 1)$

Table 2.2: A list of the Zernike polynomials most crucial to this work (Astigmatism, Defocus, Coma and Spherical Aberration), given in Cartesian coordinates.

We have an interest in four particular Zernike terms: Defocus, Spherical Aberration, Astigmatism and Coma, because they have the largest effect on visual acuity. The following is a brief overview of the optical effects of these aberrations. Of these, defocus is the most straightforward term, and represents the distance between the

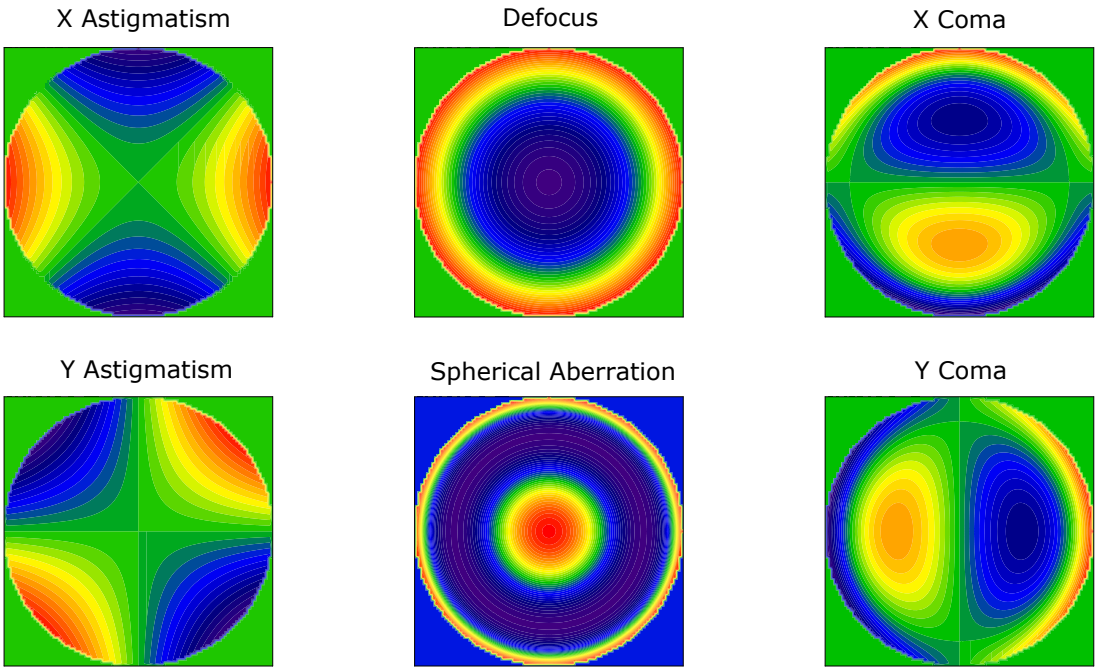

Figure 2.7: Wavefront maps of Astigmatism, Defocus, Coma and Spherical Aberration shown over the unit disk.

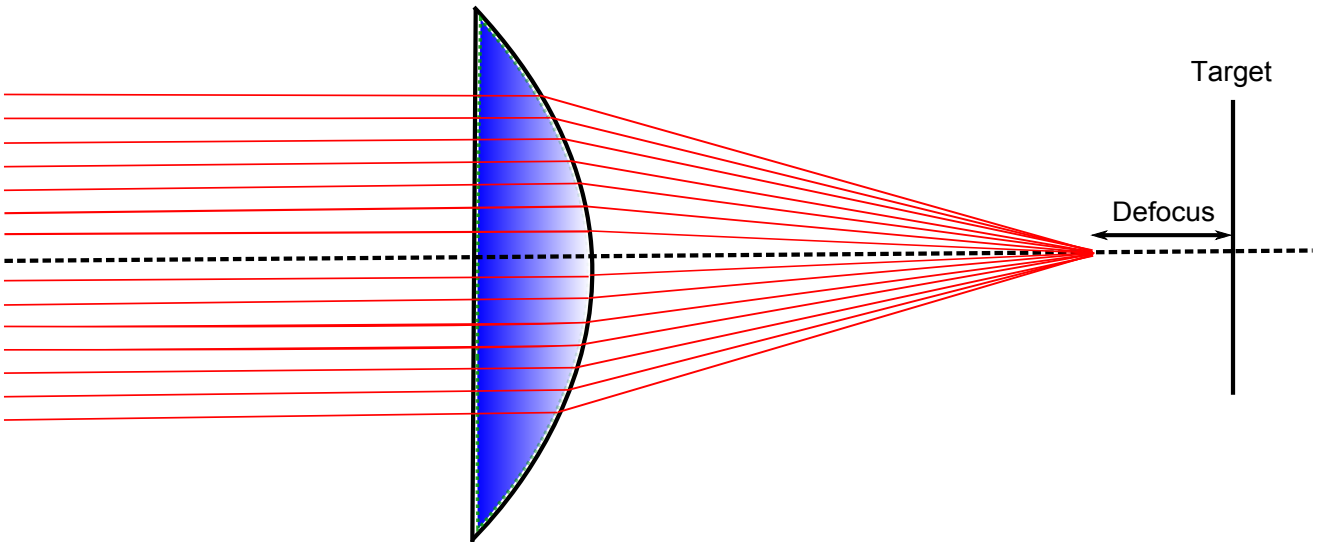

Figure 2.8: This system shows an example of defocus; the rays do not converge on the target focal point.

actual focus of an optical system and the desired focus. An example of defocus is shown in Figure 2.8.

Spherical aberration is another aberration that appears even if rays are parallel and on axis, and occurs when rays near the periphery of a system are focused with more optical or less power than paraxial rays. This means that the rays do not meet at a single focal point. Figure 2.9 shows an example of positive spherical aberration.

There are two types of astigmatism. The first, called refractive astigmatism, occurs when rays travelling in different planes have differing focal points. This is caused by the shape of the optical elements: when the lens or cornea is not rotationally symmetric about the optical axis. In Figure 2.10 one can see that the red rays in the horizontal plane are focused to a point (T_1) which has a smaller focal length than that of the blue rays in the vertical plane, focused to S_1. This can occur in the eye even with a simple model: if the cornea has a biconvex form, a difference in radius of

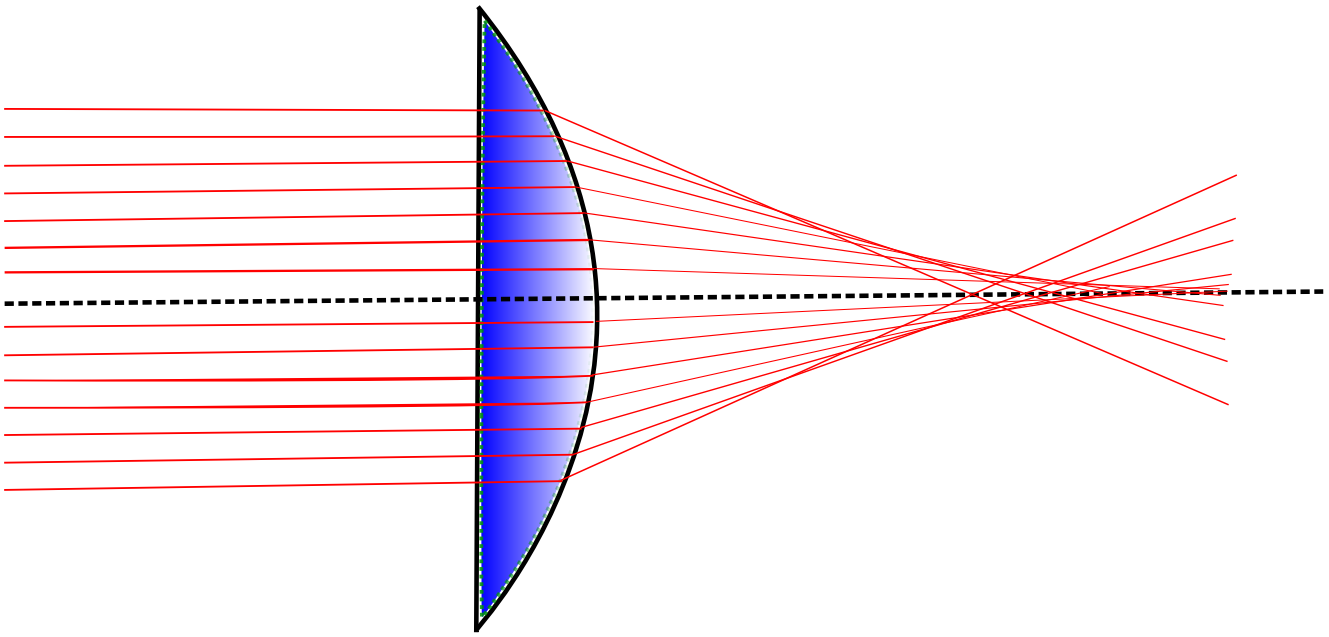

Figure 2.9: This system shows an example of positive spherical aberration; the rays at the edge of the lens are focused more strongly than the rays at the centre of the lens.

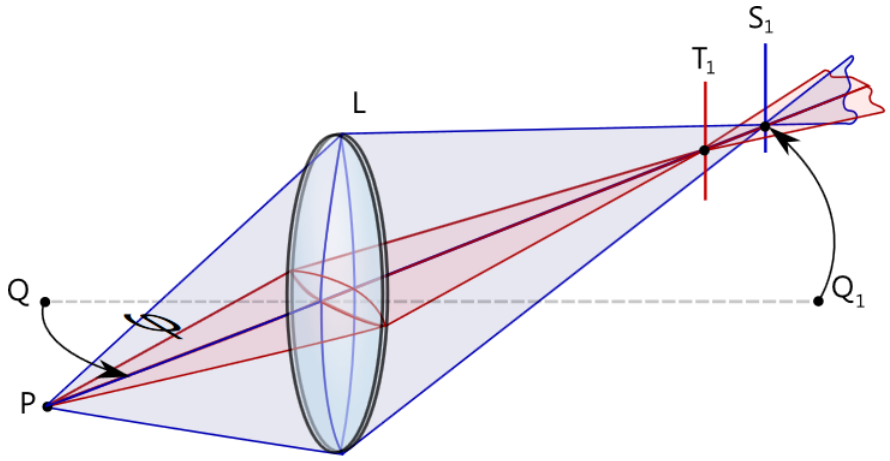

Figure 2.10: This is an example of an astigmatic lens. The blue rays one axis are focused to a different spot than the red rays on the other axis. Figure from https://en.wikipedia.org/wiki/Astigmatism

curvature or asphericity in x and y axes will cause this form of astigmatism.

The second type of astigmatism is called oblique astigmatism and occurs when objects are located off-axis from the optical axis. The effect of this is similar to refractive astigmatism, causing rays in different planes to have different focuses. The severity of this type of astigmatism varies as the angle from the optical axis increases, and is usually ignored in visual optics.

Coma is due to imperfections in an optical element or misalignment in an optical system, and occurs when off axis parallel rays are subject to different focal power. In other words, the magnification of the object is different at different parts of the lens. [52] This causes multiple focal spots for extended object, and streaking for a point light source. Figure 2.11 provides an example of a comatic lens.

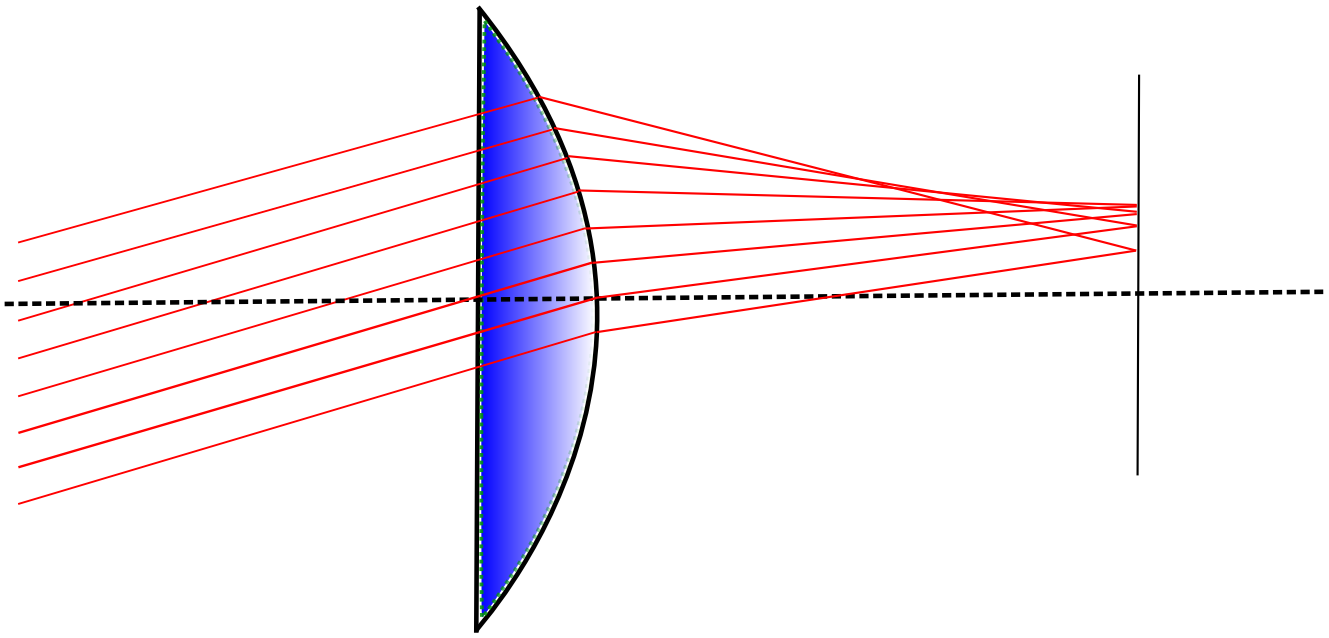

Figure 2.11: An example of a comatic lens. The off-axis parallel rays have multiple focal spots.

3 Building the Model Eye

Figure 3.1 outlines the algorithms used to obtain the eye parameters (including missing lens and GRIN paremeters) for individual patient eyes. The flow chart on the left shows the steps necessary to obtain ray tracing data. The right chart shows the overall strategy used to analyse this data. These steps will be discussed further in this chapter.

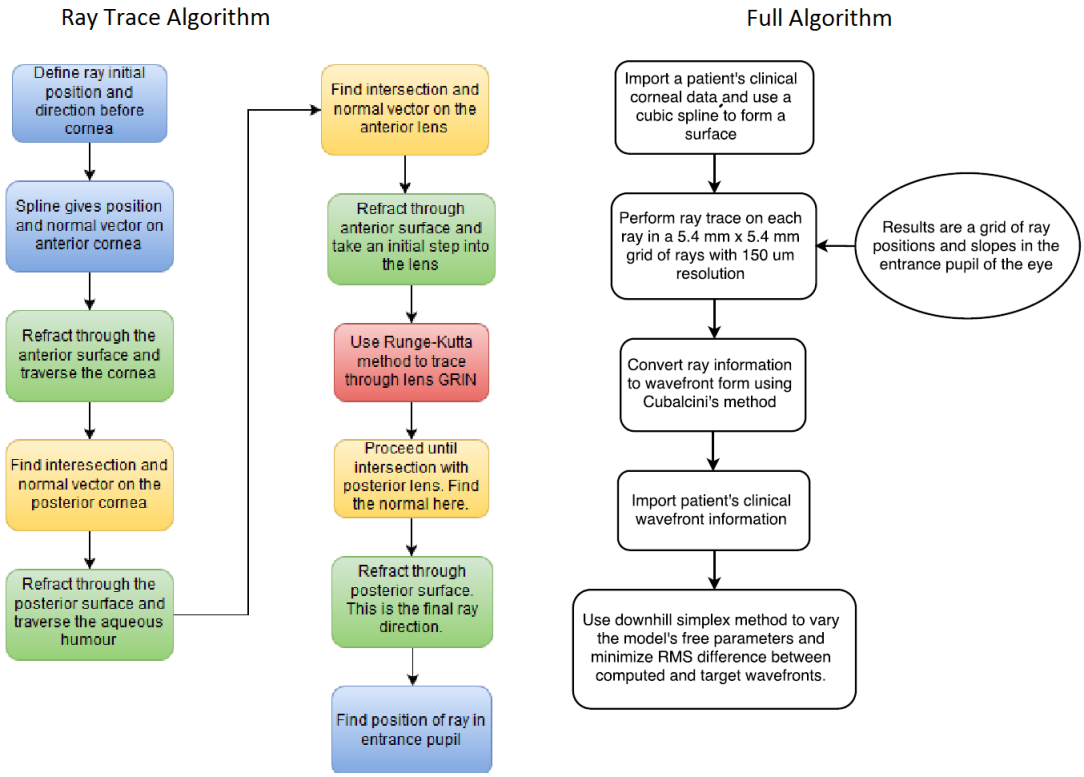

Figure 3.1: Two flowcharts representing the algorithms used in this work. The left is the algorithm used to trace rays, while the right shows the full algorithmic overview.

3.1 Simple Refraction

The general process for 3-dimensional refraction of skew rays is shown here. First, define the unit normal to the refracting surface as [53]:

$$\hat{d} = (d_x, d_y, d_z) \tag{3.1}$$

Snell's law in 3 dimensions is stated as:

$$n(\hat{v}_{incident} \times \hat{d}) = n'(\hat{v}_{refracted} \times \hat{d}) \tag{3.2}$$

Where n is the index of refraction of the incident medium, n' the index of the refracting medium, $\hat{v}_{incident}$ is the unit vector of the incident ray and $\hat{v}_{refracted}$ is the desired result: the unit vector of the refracted ray. Multiply this equation vectorially by $\hat{d}$ to yield:

$$n(\hat{v}_{incident} - \hat{d}(\hat{v}_{incident} \cdot \hat{d}) = n'(\hat{v}_{refracted} - \hat{d}(\hat{v}_{refracted} \cdot \hat{d}) \tag{3.3}$$

Expanding this into scalar form and defining (v_x, v_y, v_z) and (v'_x, v'_y, v'_z) as the components of $v_{incident}$ and $v_{refracted}$ respectively gives:

$$n'v'_x - nv_x = kd_x \tag{3.4}$$

$$n'v'_y - nv_y = kd_y \tag{3.5}$$

$$n'v'_z - nv_z = kd_z \tag{3.6}$$

as the solution, where k is defined as:

$$k = n'(\hat{v}_{refracted} \cdot \hat{d}) - n((\hat{v}_{incident} \cdot \hat{d}) = n'\cos\theta' - n\cos\theta \tag{3.7}$$

Height (cm)	Jenkins angle of refraction	Computed angle of refraction
1.0	6.8700110°	6.8700109°
2.0	13.841356°	13.841355°
3.0	21.029692°	21.029690°

Table 3.1: Ray tracing results found by Jenkins and White vs the results found by our developed software.

where finally θ and θ' are the angles of incidence and refraction respectively.

Validation of this algorithm came twofold. The first test was to reproduce a known physical lens. For this purpose, Edmund Optics lens DCX32969 [54] was used. It has two convex surfaces with 9 mm radii of curvature and no ellipticity. The central thickness is 2.60 mm. Knowing these parameters allowed us to exactly reproduce the lens computationally. The back focal length of this lens is listed in Edmund Optics catalogue as 17.12 mm, and our computational result of paraxial rays mirrored this perfectly. However, the catalogue does not include spherical aberration, so an additional test was performed to ensure the accuracy of our refraction algorithm.

Jenkins and White [52] trace rays through a surface computationally, and presents the results at each step. Since Jenkins traced rays at multiple heights, it is possible to verify the influence of the spherical aberration of the surface. The surface was spherical, with a radius of curvature of 5.0 cm. The media of refraction had indices of 1.0 for the incident and 1.672 for the refracted. Table 3.1 lists the results from this test and show that the surface refraction algorithm is working.

3.2 Anterior Cornea Spline

Topographical data of the anterior corneal surface is available clinically through the use of many different techniques. In order to use it computationally, it is necessary

to convert it into a surface via interpolation. The method used in this work is a cubic spline [55], which produces an interpolated curve with a smooth first derivative and a continuous second derivative. This method is very convenient computationally, as the gradient of the surface is calculated in the process of interpolating, and is also needed in the next step for ray tracing.

As computational time for a two dimensional case is very short, the easiest way to extend it from two to three dimensions is outlined in Figure 3.2. First, a grid of points of known functional values over the two independent axes is created. Many two dimensional splines are performed along each known value of one of the independent dimensions in order to obtain the function's result at the necessary value of the other variable. Finally, the results are splined one last time, yielding the function's value at any point in the parameter space. [55]

This algorithm was tested by creating a matrix of surface points from a known function, and comparing these values to the interpolated prediction at the same location. Known values were interpolated within a factor of approximately 10^{-6}.

3.3 GRIN ray tracing

In order to ray trace through a gradient index medium, the solution to the ray equation:

$$\frac{d}{ds}\left(n\frac{dR}{ds}\right) = \nabla n \tag{3.8}$$

must be found. Here R is the ray position vector and s is the ray direction vector along the trajectory of the ray.

There are many computational methods available to solve this (see [56–60]); the one used in this work is the Runge-Kutta method proposed by Hewak [61]. Starting with an initial position R_n and direction s_n, the position and direction at the next

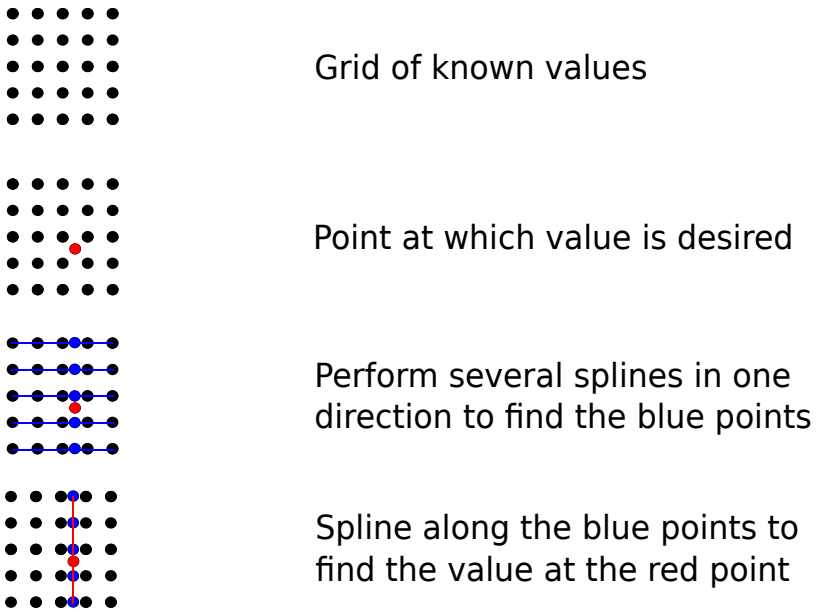

Figure 3.2: A visual representation of a simple way to extend a two dimensional spline to a three dimensional version.

step are given by:

$$R_{n+1} = R_n + h\Big(u_n + \frac{A+2B}{6}\Big) \tag{3.9}$$

$$u_{n+1} = u_n + \frac{A+4B+C}{6} \tag{3.10}$$

where h is the distance travelled along the direction vector, and A,B and C are given as follows:

$$A = h\nabla n(R) \tag{3.11}$$

$$B = h\nabla n\Big(R + \frac{hu}{2} + \frac{hA}{8}\Big) \tag{3.12}$$

$$C = h\nabla n\Big(R + hu + \frac{hB}{2}\Big) \tag{3.13}$$

The Runge-Kutta GRIN ray tracing was validated using two well-known gradient models: creating a Luneburg lens [62] (described below), and replicating the results from Liou and Brennan [11].

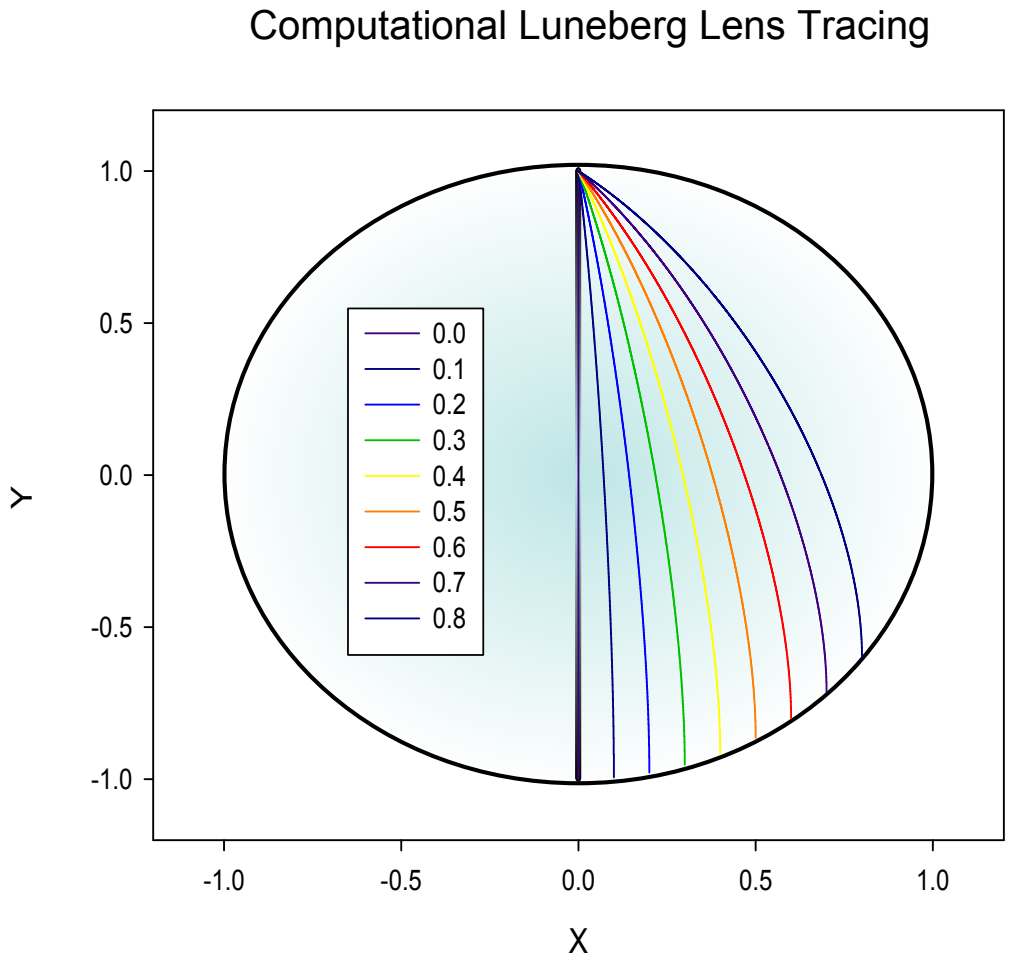

Figure 3.3: The results of ray tracing through the Luneburg GRIN lens at varying ray heights. All rays travel in the positive y-direction, and through the posterior apex of the lens.

The Luneburg lens is a spherical lens designed such that any ray parallel to the optical axis passing through it is focused through the centre of the posterior apex. The GRIN is radially symmetric with a distribution given by $n(r) = n_0(2 - r^2)^{0.5}$, where n_0 is defined to be matched to the index of the surrounding medium, and r is normalized to be 1 at the lens edge. The results of ray tracing using Hewak's solution [61] through a Luneburg lens are shown in Figure 3.3.

When this model is implemented in our software, all rays pass through the apex

Surface	Radius (mm)	Asphericity	Position on Optical Axis (mm)
Anterior Cornea	7.77	-0.18	-3.66
Posterior Cornea	6.40	-0.6	-3.16
Anterior Lens	12.40	-0.94	0.0
Posterior Lens	-8.10	0.96	4.02

Table 3.2: The parameters of the cornea and lens used by Liou and Brennan.

of the posterior portion of the lens. The error on this computation was equal to the step size through the GRIN, which is the expected result.

Next, the average eye studied by Liou and Brennan was traced. The parameters of the cornea and lens of this eye are as listed in Table 3.2. Our computational verification used an identical cornea, lens and GRIN as suggested by Liou, and looked at the transverse spherical aberration of rays at 1.0, 2.0, 3.0 and 4.0 mm ray heights. Our software found values within the error of their plots. (They do not list their values, rather they plot it with large symbols. The results of their study are highly regarded, so this was tried as an approximate test. The exact values they found are unknown).

3.4 Cubalchini Method

In order to determine the coefficients of aberration for our model eye, the method presented by Cubalchini [63] was used. This is an RMS method used to fit data with orthogonal polynomials. First we define the directional derivatives of the wavefront as:

$$P(x,y)_i = \frac{\partial \phi(x,y)_i}{\partial x} \tag{3.14}$$

$$Q(x,y)_i = \frac{\partial \phi(x,y)_i}{\partial y} \tag{3.15}$$

P and Q are represented physically as the x and y components of the final ray direction vector. Note that throughout this derivation, $(x, y)_i$ refers to the original position of ray i in the entrance pupil. A measurement vector R, an estimator, is constructed with P and Q as:

$$R = (P(x,y)_1, P(x,y)_2, ..., P(x,y)_k, Q(x,y)_1, Q(x,y)_2, ..., Q(x,y)_k)^T \tag{3.16}$$

The length of this vector is $2n$, where n is the total number of rays traced (as there is an x and y direction component for each ray). The goal is to use this estimation vector in order to determine a vector of constants $\hat{A} = (\hat{a_2}, \hat{a_3}, \cdots, \hat{a_i})$ that define the wavefront as:

$$\Phi(x,y) = \sum_{i=2}^{I} \hat{a}_i Z_i(x,y) \tag{3.17}$$

We use the Zernike polynomials as our set of Z's, though any orthogonal set of functions would work. The term for $i = 1$ is skipped as it is a constant in the Zernikes (with a 0 derivative). In order to retrieve our wavefront, $\hat{A}$ must be chosen such that the error squared between the estimates and measurements is minimized. There is a minor difference in this step from the usual process, as our measurement vector uses only the directional derivatives, so we must also minimize the error from the derivatives of the Zernikes:

$$\frac{\partial \Phi(x,y)}{\partial x} = \sum_{i=2}^{I} \hat{a}_i \frac{\partial Z_i(x,y)}{\partial x} \tag{3.18}$$

and

$$\frac{\partial \Phi(x,y)}{\partial y} = \sum_{i=2}^{I} \hat{a}_i \frac{\partial Z_i(x,y)}{\partial y} \tag{3.19}$$

Then the minimization function is given as:

$$F = \sum_{k=1}^{K} \left[\left(P(x,y)_k - \sum_{i=2}^{I} \hat{a}_i \frac{\partial Z_i(x,y)}{\partial x} \right)^2 + \left(Q(x,y)_k - \sum_{i=2}^{I} \hat{a}_i \frac{\partial Z_i(x,y)}{\partial y} \right)^2 \right] \tag{3.20}$$

Next, F must be minimized with respect to $\hat{A}$, resulting in:

$$\begin{aligned} &\sum_{k=1}^{K} \left(P(x,y)_k \frac{\partial Z_j(x,y)_k}{\partial x} + Q(x,y)_k \frac{\partial Z_j(x,y)_k}{\partial y} \right) = \\ &\sum_{i=2}^{I} \left[\hat{a}_i \sum_{k=1}^{K} \left(\frac{\partial Z_j(x,y)_k}{\partial x} \frac{\partial Z_i(x,y)_k}{\partial x} + \frac{\partial Z_j(x,y)_k}{\partial y} \frac{\partial Z_i(x,y)_k}{\partial y} \right) \right] \end{aligned} \tag{3.21}$$

Where $j = 1, 2, ..., I$. This rather unwieldy expression is best written in an alternative matrix notation:

$$DR = E\hat{A} \tag{3.22}$$

where

$$D = \begin{pmatrix} \frac{\partial Z_2(x,y)_1}{\partial x} & \frac{\partial Z_2(x,y)_2}{\partial x} & \cdots & \frac{\partial Z_2(x,y)_K}{\partial x} & \frac{\partial Z_2(x,y)_1}{\partial y} & \cdots & \frac{\partial Z_2(x,y)_K}{\partial y} \\ \frac{\partial Z_3(x,y)_1}{\partial x} & \frac{\partial Z_3(x,y)_2}{\partial x} & \cdots & \frac{\partial Z_3(x,y)_K}{\partial x} & \frac{\partial Z_3(x,y)_1}{\partial y} & \cdots & \frac{\partial Z_3(x,y)_K}{\partial y} \\ \vdots & \vdots & \ddots & \vdots & \vdots & \ddots & \vdots \\ \frac{\partial Z_i(x,y)_1}{\partial x} & \frac{\partial Z_i(x,y)_2}{\partial x} & \cdots & \frac{\partial Z_i(x,y)_K}{\partial x} & \frac{\partial Z_i(x,y)_1}{\partial y} & \cdots & \frac{\partial Z_i(x,y)_K}{\partial y} \end{pmatrix} \tag{3.23}$$

and:

$$E = DD^T \tag{3.24}$$

Finally, we have an explicit expression for the Zernike polynomial fit:

$$\hat{A} = E^{-1}DR = (DD^T)^{-1}DR \tag{3.25}$$

Validation for the implementation of this method came from manually computing slopes of rays from a known wavefront using the derivatives of the Zernike polynomials. These slopes were fed into the Cubalchini algorithm, and results matched the initial wavefront within computational error. This was tested with both simple (e.g. defocus only) and complex wavefronts (e.g. arbitrary values for all 27 polynomials).

The inherent limitation in this method is the same reason it is convenient: it fits using the derivatives of the Zernike polynomials (i.e. in the case of this study, the ray slopes) rather than the Zernikes themselves. The derivatives are not orthogonal functions. This can lead to potential cross correlation between terms. Most clinical aberrometers use a similar methodology, so it should not adversely effect the results of this study.

3.5 Downhill Simplex Method

Once the Zernike coefficients of the model's wavefront have been established using Cubalchini's method, there must be an attempt to minimize the difference between the computed values and the known values of the patient's optical quality. In order to do this, the multidimensional downhill simplex method [55] is used to search parameter space for values which best replicate the known optical aberration of the patient.

There are two chief benefits to the simplex method over other fitting methods. Firstly, it requires only the evaluation of the function, and not its derivatives. Secondly, it is simple in application. This method is not computationally efficient, but is acceptable in this work as the overall computational cost is low.

For a parameter space of N variables, a simplex is defined as an N dimensional shape of $N + 1$ points with unique values in parameter space and their connecting line segments and faces. The algorithm evaluates a merit function at each of the

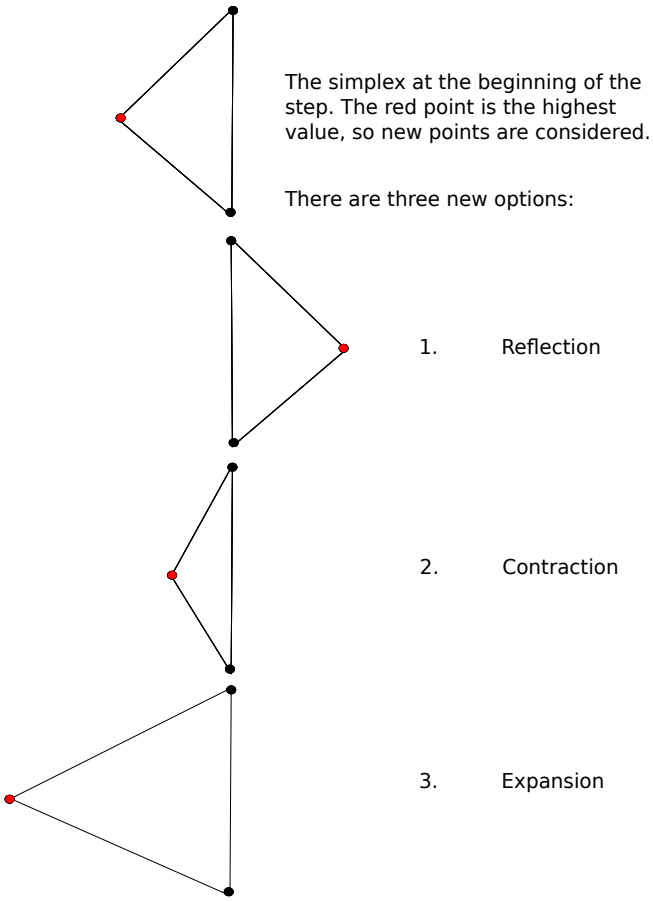

Figure 3.4: The three possible steps for the simplex method to take. The algorithm ends when all three vertices are under the specified error tolerance.

points of the simplex. In our case, this merit function is defined as the root mean square (RMS) error of the computed wavefront compared to the patient's measured wavefront. The algorithm takes the worst evaluated point and attempts to move it to a place in parameter space deemed better by the merit function. It evaluates 3 new locations: the first a reflection of the point, the second a contraction of the point towards the simplex, and the third an expansion of the point away from the simplex. This step is demonstrated in Figure 3.4. For simplicity, it is shown here in 2 dimensions, though this work uses 3.

We define the RMS merit function of a simplex of parameters to be:

$$RMS = \sqrt{\frac{1}{n}\sum_{i=0}^{n}\left((P_i - P_{ir})^2 + (Q_i - Q_{ir})^2\right)} \tag{3.26}$$

where n is the total number of rays, and P_i and Q_i are the computed x and y ray directional components of each ray. P_{ir} and Q_{ir} are the real x and y ray directional components of each ray at the same initial positions as the equivalent computed ray. These real values are calculated using the clinically measured wavefront we wish to fit the lens to. The RMS of a set of parameters sums to zero if the slopes of the rays produced by our computational eye are identical to the slopes given by the target wavefront.

The end condition of the simplex algorithm is decided by inputting an error tolerance, and in this case, both an absolute value and a relative value were implemented. The absolute tolerance is defined such that when the RMS value of any simplex vertex becomes low enough, the algorithm ends, outputting the parameters at this vertex. The relative value is designed to stop the algorithm if the RMS of the vertices of the simplex come within a given percent value of each other. The relative error end condition is implemented to prevent the algorithm from never finishing in the case of eyes which cannot be fitted perfectly with available parameters.

In order to validate the efficacy of this fitting procedure, the wavefront was found for an eye with known parameters. Following this, the eye parameters were reset to initial guesses, and the simplex method was engaged. This was repeated many times over a large scan of parameter space, testing 1500 eyes with W ranging from 2 to 8 and q_{pos} from -1.5 to 1.5. Other than these parameters, an average cornea and lens were chosen. The results show that the fitting algorithm reproduced the parameters within 1% accuracy in every case, which was the pre-defined stop condition.

4 Testing the Eye Model

From the previous chapters, we see that the eye model requires many parameters (see Figures 2.1 and 2.2) to be fully specified. Many of theses are available from biometry, which leaves only a few lens paramters to find in order to customize the eye model to an individual eye.

4.1 Methodology

A population of refractive surgery candidates with full biometry information would be an ideal case to test our lens model. In these patients, the cornea is laser ablated to change shape and optical properties. If the cornea is the only element of the eye that has changed, then any lens that successfully predicts refractive behaviour of the full eye prior to surgery should also be able to predict the behaviour of the full eye after surgery. This means that the lens model proposed in this thesis can be deemed valid on an individualized level if a fitted pre-surgical lens can predict the results of a refractive surgery.

The accuracy of the model's results will be compared to the most common method used for predicting refractive outcomes, which was first suggested by Artal in 2003 [64]. Artal suggests that the eye's optical properties can be the sum of two phase plates at the eye's entrance pupil; one of the anterior cornea and one for the other surfaces, the internal aberrations. We consider the pre-operation eye without a lens, looking only at the wavefront produced by the cornea. The difference between the wavefront shown by the cornea and that of the full eye is an estimation of the internal aberrations. The resulting estimation is used in the post-operation eye with the new cornea. The generated wavefront serves as a standard against which the results of our model will compete. This approach is referred to as the phase plate approximation.

As our model is still in the preliminary stages of testing, it is important to get an assessment without spending a surfeit of resources, so we must rely on available data to perform an initial evaluation. This project will use data from a study performed at the University of Ottawa Eye Institute, assessing the performance of a new (at the time) surgical algorithm by comparing pre and post-operative data. The study population was divided into two test groups, the control and retreat. The control group are new patients receiving a first ever refractive surgery, whereas the retreat group consists of patients whose initial surgery did not meet expectations and a second treatment was performed to improve the outcome.

Unfortunately, these studies did not collect full biometric data as it was unnecessary for the study. The data available to us for use in this work is anterior corneal topographical maps, pupil size, and full ocular wavefront information (up to the 7th order Zernike coefficient), both pre and post-operation.

Because there is no eye length included in the patient information, the exact source of defocus is unknown. When setting eye parameters, the power of the lens is needed, which in a full biometry would be obtained from eye length and defocus from the wavefront. As eye length is unknown, there are two possible approaches.

In the first approach, the retina is located at exactly the average eye length. However, the light travelling the eye is not focused onto this plane. In this case, the assumption made is that the patient's eye is the average length, and the defocus perscription is due to the refractive power of the lens and cornea. This will be referred to as lenticular defocus.

The second approach assumes that the eye focuses light onto the average focal plane. However, the retina is not located in this plane; the patient's eye is not the same size as the human average. This approach will be called axial defocus. (Figure 4.1)

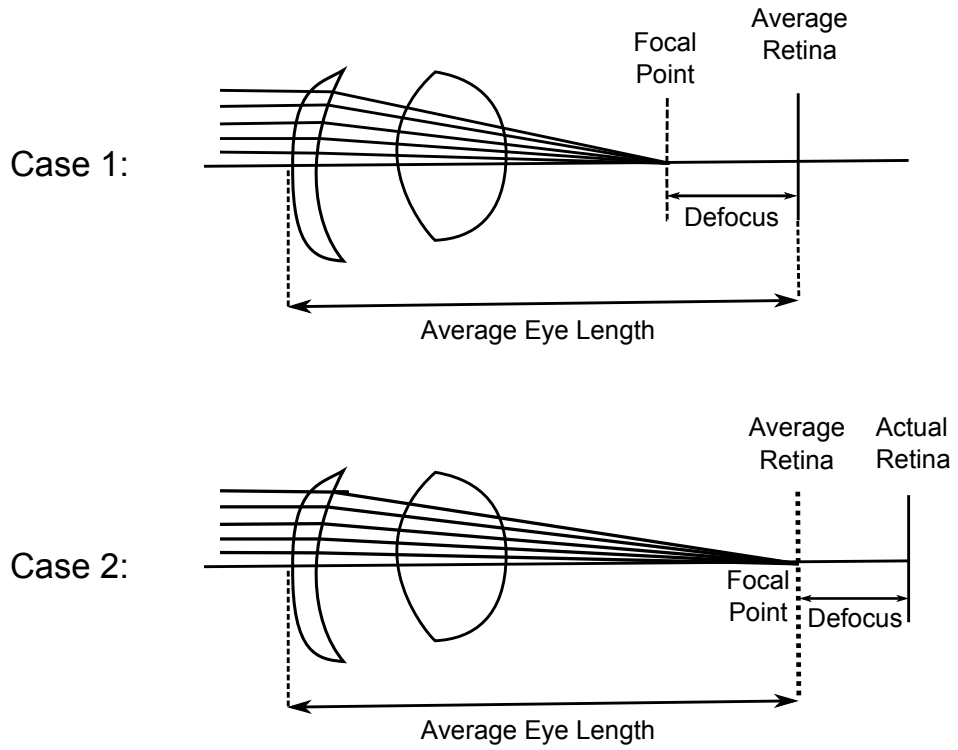

Figure 4.1: The two approaches of defocus. The first case assumes that the retina is at the average eye length. The second assumes that light is focused at the average eye length, and the defocus refers to the deviation of the patient's eye length from the average. Note that elements and refraction in this diagram are not to scale.

In reality, most patients will have a mix of both cases (i.e. neither an average retina nor perfectly focused light), contributing to defocus, but there is no way to distinguish this as the patient's eye length is not known in this study.

The patient's eye will be built following the process described in Chapter 2. First, the corneal topography will be splined into a refracting surface. Next, the full eye will be ray traced using an average lens. Wavefront information will be extracted from the ray data using the method outlined by Cubalchini. Finally, the RMS error between the known wavefront aberration of the patient and the computed value of the model eye will be minimized by varying lens parameters using the downhill simplex method.

4.2 Choice of Parameters

Preliminary tests in fitting defocus and spherical aberration assumed that the lens had an average anterior apical radius of curvature, allowing us to use biometric relationships to find the rest of the lens parameters. The only parameters that were allowed to vary were W and posterior lens asphericity (as the biometric relationship here was not statistically strong enough). However, it was found that fitting defocus or spherical aberration was impossible with only these parameters floating.

The statistically weakest biometric relationship used inferred the value of lens anterior asphericity from lens anterior radius of curvature. This was allowed to float for the next attempt. Even still, it was not possible to achieve both spherical aberration and defocus in the same fit with an average lens anterior radius of curvature. Finally, we settled on scanning through posterior corneal asphericity and anterior lens curvature rather than taking the average value. This was chosen over floating these parameters so that they did not vary from the average too significantly, which is especially important for the anterior lens curvature as other parameters are inferred

Measured	Biometry	Average	Fitted	Scanned	Unknown
Cornea r_{ant}	b	Cornea r_{pos}	W	Lens r_{ant}	Eye length
Cornea q_{ant}	Lens r_{pos}	a_1	Lens q_{ant}	Cornea q_{pos}	
Pupil radius		a_2	Lens q_{pos}		
Wavefront		n_s			
		n_c			
		C_0			
		C_1			
		C_2			

Table 4.1: A list of the source of parameters for our eye model. Values listed in the measured column were taken clinically by the OHRI. Parameters in the biometry column were found using statistical biometric relationships, and values in the average column are the average value of that parameter in the human eye. The values from the fitted column were free to float using the Simplex method, and the scanned column means the fit was repeated many times over the range of this parameter. Eye length was unknown throughout this study.

from it. This allowed both defocus and spherical aberration to be fit simultaneously. Posterior corneal radius was kept at the average value, and b and posterior radius of curvature were found using biometric relationships (which have very high statistical significance).

Next, we look at the influence of lenticular parameters on astigmatism and coma. While these aberrations are very important considerations for visual clarity, it was not immediately clear whether they should be used as values to assess our model. The change made by every parameter under consideration for the lens model is circularly symmetric, while the two aberrations discussed are not. To test whether they were strongly affected by a varying lens, and whether they indicated a good or bad fit of the lens, r_{ant},W,q_{ant} and q_{pos} were scanned through the observed ranges in human

Patient	Highest Astigmatism Change	Highest Coma Change
G1	2.01%	3.12%
G2	3.30%	4.07%
G3	3.55%	1.72%
G4	4.77%	4.44%

Table 4.2: r_{ant},W,q_{ant} and q_{pos} of the lens are scanned through (over 1500 versions of each lens tested) and the value of astigmatism and coma are recorded. This table shows the difference between the lowest and highest result for these aberrations.

eyes (Table 1.1). The overall changes in astigmatism and coma were recorded and reported in Table 4.2.

The highest variation of astigmatism was found to be 4.77% and the highest variation of coma was found to be 4.44%, indicating that varying our considered lens parameters will not be sufficient to predict these aberrations. Astigmatism is mainly corneal; beyond the clinical measurement of the anterior surface of the cornea, this thesis does not consider other provisions to fit this aberration. We use an on-axis point source of light with well aligned optics (with the potential for a future model to explore misaligned optics), so coma is also not used for fitting. The success of the initial test of our model lens should not depend on whether these aberrations are well predicted. For the remainder of this document, the ability to predict defocus and spherical aberration will be considered as the main indicator of success.

4.3 Control Patients

Presented in this section are the results from the control group:

Table 4.3 gives the clinical and model defocus and spherical aberration for each control patient's pre-surgery fit, and Table 4.4 shows the lens parameters that yield

Patient	Computed Def. (D)	Target Def. (D)	Computed SA (μm)	Target SA (μm)
G1	2.300	2.300	-0.0168	-0.0167
G2	3.754	3.740	0.1036	-0.0422
G3	4.380	4.380	0.1770	0.1770
G4	3.600	3.600	0.2440	0.2440

Table 4.3: Defocus and spherical aberration results of best pre-operation fits for control patients.

Patient	W	q_{ant}	q_{pos}	r_{ant} (mm)	q_{cornea}
G1	95.00	-12.91	-30.82	8.4	0.6
G2	1.170	-3.435	-4.219	8.2	0.6
G3	2.529	0.2578	-5.599	10.6	0.0
G4	2.912	2.490	-1.698	8.8	0.6

Table 4.4: Results of all varied parameters of best fits for control patients.

these values. The model matches defocus within ±0.015 D for every control patient. Similarly, we can reproduce spherical aberration within ±0.001 μm except for patient G2, where SA deviates by 0.15 μm. Also of note is that patient G1 has fitted parameters that are outside the expected physical ranges of the human eye (as seen in Table 1.1), with $W = 95.00$, $q_{ant} = -12.91$, and $q_{pos} = -30.82$. This will be discussed further in section 5.3.

Figures 4.2 and 4.3 show the error in defocus and spherical aberration respectively when the full eye's wavefront is computed with the post-operation cornea and the lens fit to the pre-operation values. This data will be key to determining the validity of the proposed lens model. For all patients tested, both the defocus and spherical aberration are shown to be close to or above the threshold for clinical error - 0.25 to 0.5 D for defocus, and approximately 0.05 μm SA.

The surgical procedure corrected between 2.0 and 2.5 D for the control patients when they had a range of 2.5 to 3.3 D of defocus prescription. The error on fits ranged between 0.25 and 2.0 D, which is between 10% and 80% of the corrected defocus. Due to limitations of laser eye surgery at the time of the Ottawa Eye Institute study, the spherical aberration of patients' increased due to the surgery. The range for the control patients increase in SA was 0.05 μm to 0.25 μm. The error in fit had an identical range, showing in some patients a mismatch of 100% of the expected change. These high values indicate that something missing from our approach: this will be discussed further in Chapter 5.

4.4 Retreat Patients

Next are the results from the group of retreat patients:

Presented in Table 4.5 and Table 4.6 are the clinical and model defocus and

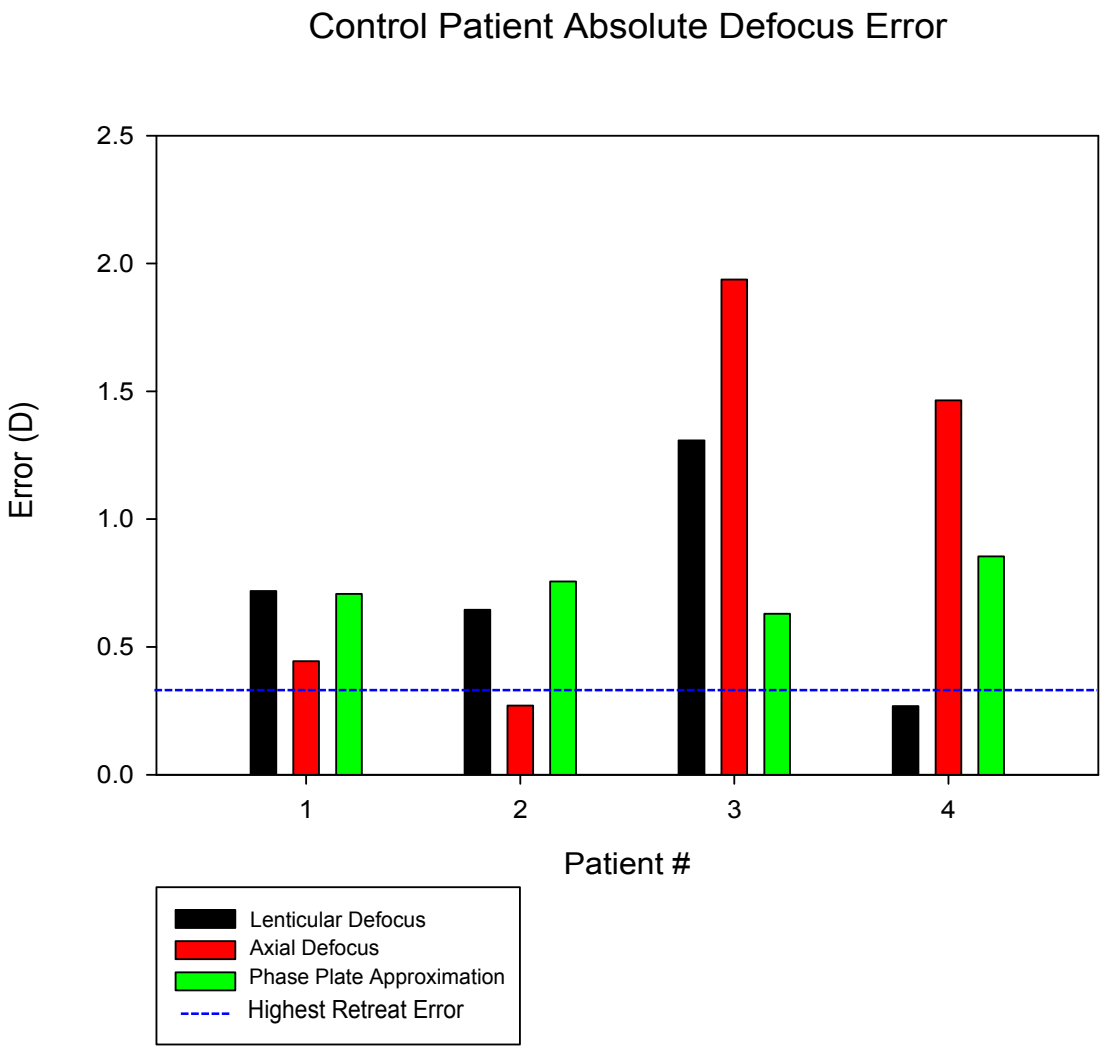

Figure 4.2: Error in predicted residual defocus following refractive treatment of control patients. The black bar shows the error from the lenticular defocus approach and the red shows the axial defocus approach, while the green bar represents the error predicted using the phase plate approximation. The dashed blue line shows the highest value of error obtained in the retreat case.

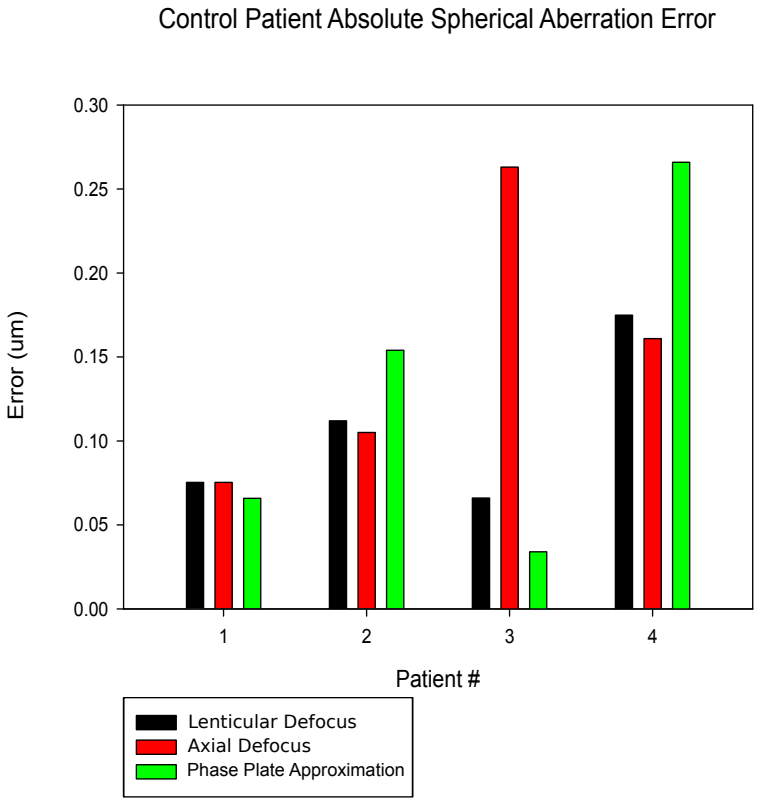

Figure 4.3: Error in predicted residual spherical aberration following refractive treatment of control patients. The black bar shows the error from the lenticular defocus approach and the red shows the axial defocus approach, while the green bar represents the error predicted using the phase plate approximation.

Patient	Computed Def. (D)	Target Def. (D)	Computed SA (μm)	Target SA (μm)
R1	1.700	1.700	0.4390	0.4390
R2	1.290	1.290	0.2850	0.2850
R3	2.400	2.400	0.3560	0.3560
R4	2.284	2.280	0.4021	0.3120

Table 4.5: Defocus and spherical aberration results of best pre-operation fits for retreat patients.

Patient	W	q_{ant}	q_{pos}	r_{ant} (mm)	q_{cornea}
R1	1.504	0.9422	-3.650	8.2	0.6
R2	3.208	4.060	-2.402	10.0	0.6
R3	2.601	1.779	-2.669	8.2	0.6
R4	1.178	0.6381	-4.261	8.0	0.6

Table 4.6: Results of all varied parameters of best fits for retreat patients.

spherical aberration for each retreat patient's pre-surgery fit, and the parameters that give these results. Defocus is again reproduced very accurately, with under ± 0.005 D error for every patient. Spherical aberation is similarly modeled, with an error range of ± 0.0001 μm, though patient R4 shows an SA mismatch of 0.09 μm. The lens parameters are all well within normal physiological ranges for these patients.

Figure 4.4 and 4.5 show the error in defocus and spherical aberration respectively when the full eye is computed with the fitted pre-operation lens and the post-operation cornea. In contrast with the control group, every patient in the retreat group shows results that are at or lower than the threshold of clinical error.

For the retreat group, the surgical procedure corrected approximately 1.5 D of defocus in each patient, which was close to the desired correction in each case. The error in defocus fit was found to be between 0.1 and 0.3 D, or on average about 20% of surgical change. In the case of spherical aberration, the patients received an increase to their prescription of 0.1 to 0.2 μm, while the range of error on SA fit is 0.02 to 0.07 μm, again around 20-30% of the surgical change. These errors are better than those seen in the control group.

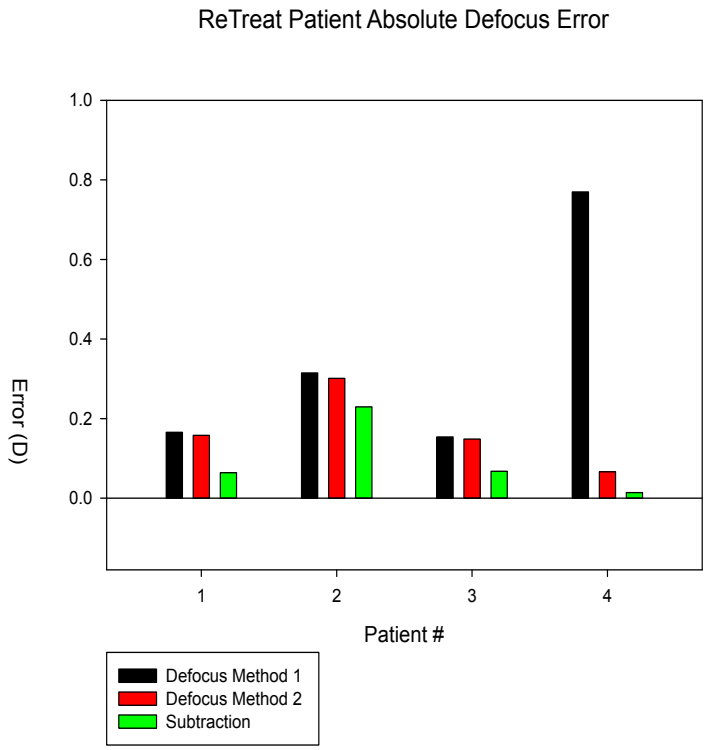

Figure 4.4: Error in predicted residual defocus following refractive treatment of retreat patients. The black bar shows the error from the lenticular defocus approach and the red shows the axial defocus approach, while the green bar represents the error predicted using the phase plate approximation.

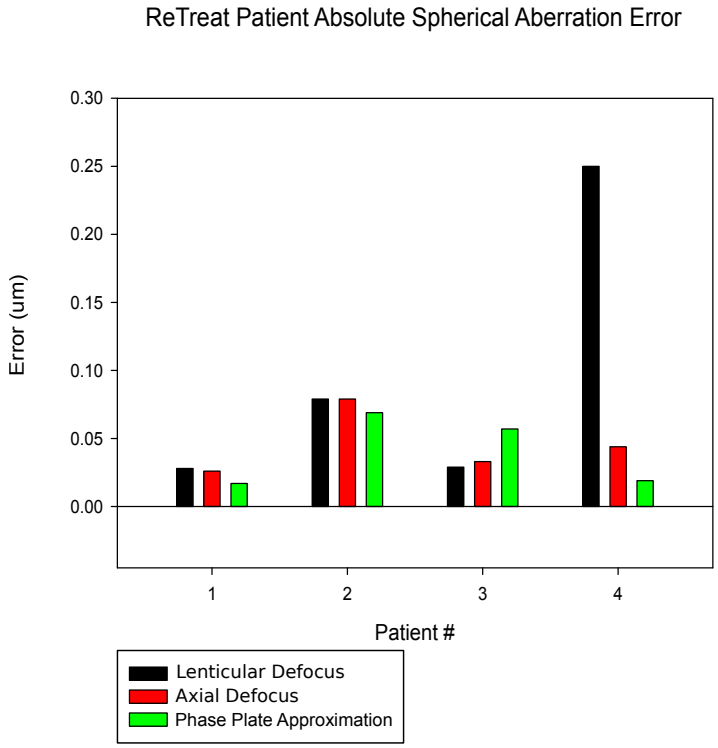

Figure 4.5: Error in predicted residual spherical aberration following refractive treatment of retreat patients. The black bar shows the error from the lenticular defocus approach and the red shows the axial defocus approach, while the green bar represents the error predicted using the phase plate approximation.

5 Comparisons to post operative outcomes

5.1 Phase plate approach

The clinical standard for error in measuring defocus is 0.25 to 0.5 D. The phase plate approximation's errors ranges from 0.6 D to 0.9 D (seen in Figures 4.2 and 4.4); outside of the clinically appropriate range. The predictions made by our model have a higher variance, with an error range of 0.25 D to 2 D, but are still only clinically acceptable at the lowest values.

In terms of SA, the predictions made by both the phase plate approximation and our model have errors ranging from 0.05 to 0.25 μm. The measurement uncertainty of most clinical instruments is in the range of 0.05 μm for spherical aberration. When considering the propagation uncertainty (the target values are not certain), we chose an error range of 0.07 μm from the target as acceptable. Spherical aberration is thus fit well in only the lowest error cases. Since both our model and the phase plate approximation have failed to reproduce the post-operation defocus or spherical aberration of the control group accurately (see Figures 4.3 and 4.5), there must have been an unaccounted for change induced by the surgery. This will be discussed in the next section.

In the case of the retreat study, the results are improved for both our computations and the phase plate approximation. All defocus predictions made by our model are under 0.3 D error, which is within acceptable clinical significance. However, the phase plate approximation has predictions that are 0.1 D better on average than the ones made by our model.

In terms of spherical aberration, the same pattern is shown. The error of every value predicted by our model is at the upper bound for SA uncertainty or better. Again, the phase plate approximation is better by about 0.01 μm on average.

5.2 Variation of Posterior Cornea

It is clear from the poor predictions by both our model and the phase plate approximation that there must have been a further change induced by the refractive surgery. As suggested by Marcos in 2001 [65], we attribute this a surgically induced variation in the posterior cornea. Throughout the fitting procedure, the posterior corneal radius of curvature has been kept constant at the average value.

In order to test this hypothesis, a scan through posterior corneal radius of curvature and asphericity was performed. This scan computed 70 different surfaces, and covered ± 0.7 of the fitted asphericity values and $\pm 0.8mm$ of the average radius of curvature value. This range was sufficient to find a global minimum of the RMS (see section 2.4 for the physical definition) for all but one patient. For the control group, Figure 5.1 shows the resulting RMS error map, and Figures 5.2 and 5.3 shows the new values for defocus and spherical aberration found at the best surface.

For every patient, adjusting the posterior cornea slightly (± 0.5 asphericity and ± 0.6 mm radius of curvatutre) was able to significantly improve the RMS error. Each control patient shows that defocus was found within 0.1 D. However, the results for spherical aberration are mixed; two patients sacrificed SA accuracy with posterior corneal adjustment in order to improve defocus, while two patients found an increase in predicted accuracy of defocus and SA. The notable case of G3 had a very large drop in accuracy of 0.5 μm for spherical aberration, although it also showed the highest improvement in defocus error at 1.9 D.

For the retreat group Figure 5.4 shows the posterior corneal adjustment map of RMS error, and Figures 5.5 and 5.6 shows the new values for defocus and spherical aberration found at the best surface compared to the previous fits. In this group, taking the best RMS value in the posterior corneal scan for each patient allowed us

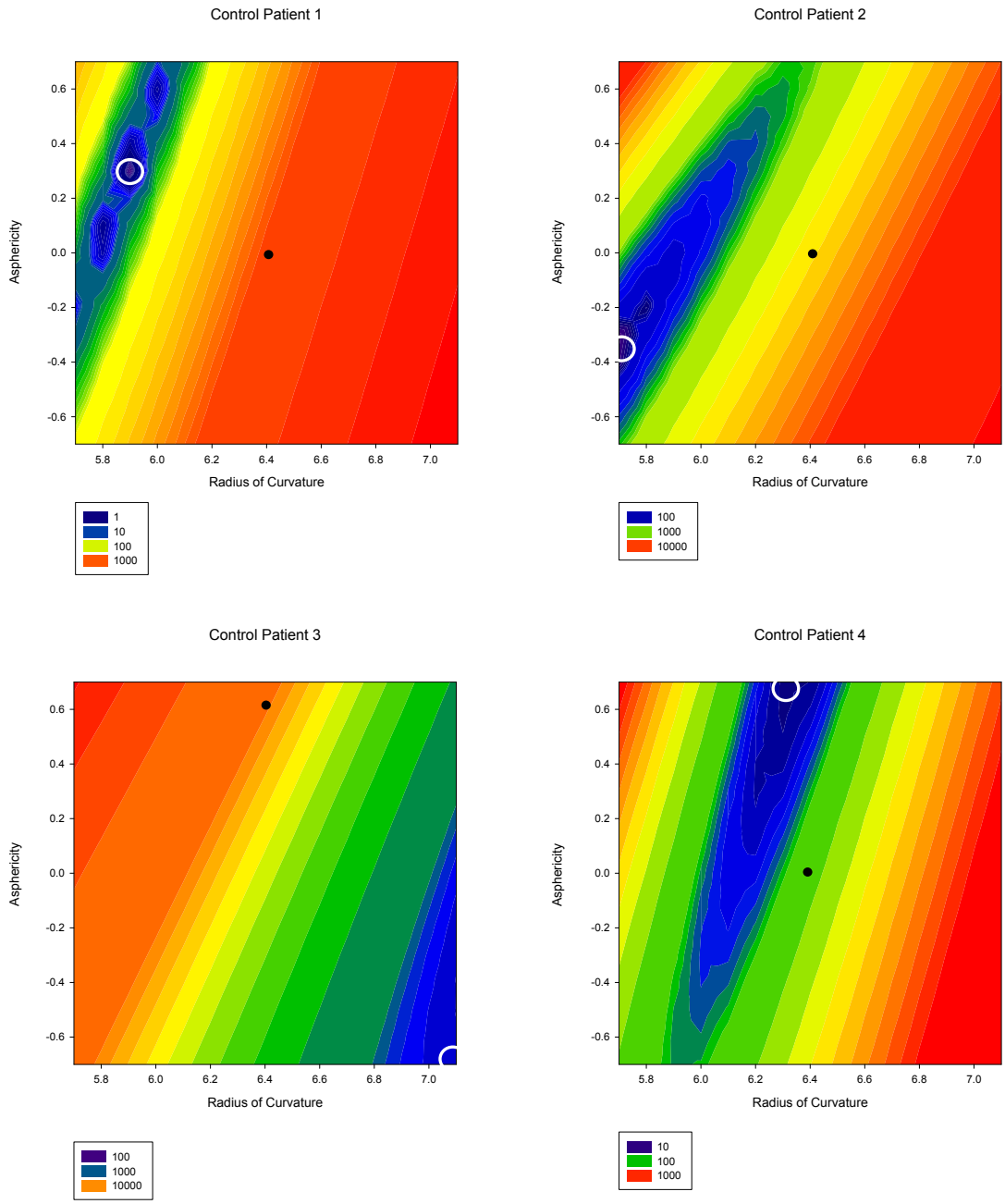

Figure 5.1: Values of RMS error (arbitrary units) shown as the posterior cornea varies over radius of curvature and asphericity for each control patient. The black spot represents the parameters where the original data were taken. The best result due to adjustment is shown within the white circle.

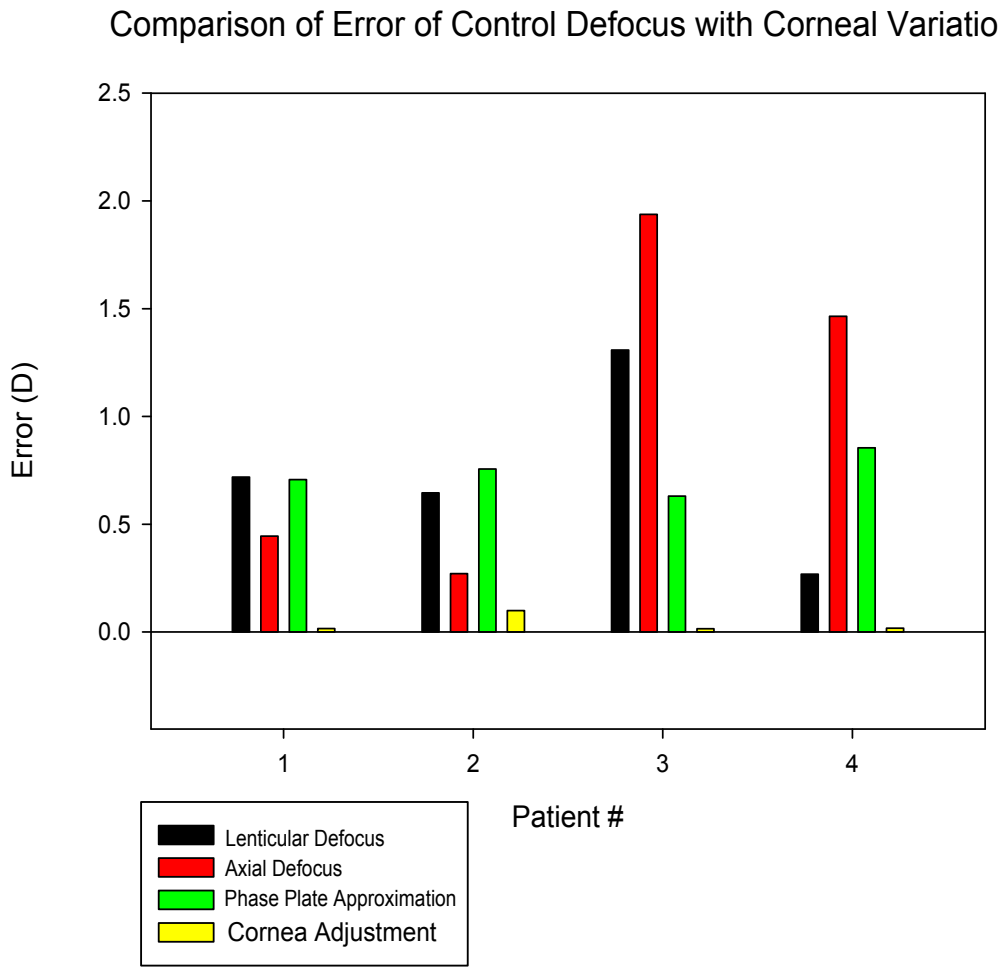

Figure 5.2: A comparison of predicted error of control patients' defocus versus error when the cornea is allowed to vary. Yellow bars show the comparison of the new defocus when the posterior cornea is varied slightly to the previous fits for the control group.

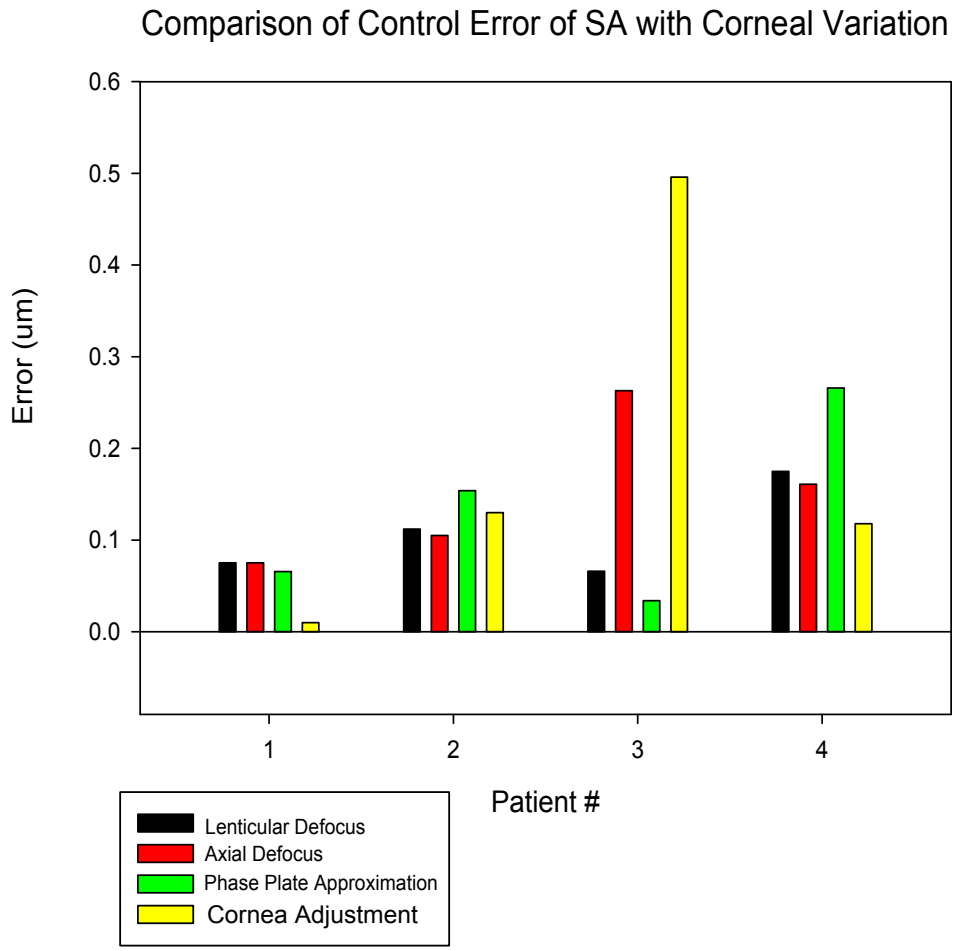

Figure 5.3: A comparison of predicted error of control patients' spherical aberration versus error when the cornea is allowed to vary. Yellow bars show the comparison of the new spherical aberration when the posterior cornea is varied slightly to the previous fits for the control group.

to minimize the defocus error to 0.05 D or less for all post-operation cases. Unlike the control case, none of the values for spherical aberration showed a decrease in accuracy; all predicted SA error remained constant or improved.

5.3 Discussion

One question raised by the fitted post-operation wavefronts is the differences between fit quality of the control and retreat groups without adjustment to the posterior cornea. The control group showed that neither defocus approach nor the phase plate approximation could accurately reproduce the patients' wavefronts. However, the retreat case was fit well within established clinical standards for both our methods and the phase plate approximation.

The difference between the two groups can be explained by the differing scope of their surgical procedures. The control patients, receiving their first surgery, had larger refractive errors (average prescription of 3.51 D) than the retreat group (average prescription of 1.92 D). As such, the control group needed more corneal tissue removal, which affects the mechanical integrity of the cornea and results in a reshaping of the posterior surface. The retreat patients had less significant refractive surgeries in comparison, resulting in lesser posterior changes.

When a slight variation of the posterior cornea was included in the methodology, there was only a single patient whose predicted values did not fall within desired clinical error: patient G3. One potential explanation is the fact that a minimum was not found when the shape of the posterior cornea was varied slightly, which could be remedied by expanding the parameters of this scan.

An important consideration that has not yet been discussed is whether the fit parameters are physiologically realistic. The obvious case to look at for this discussion

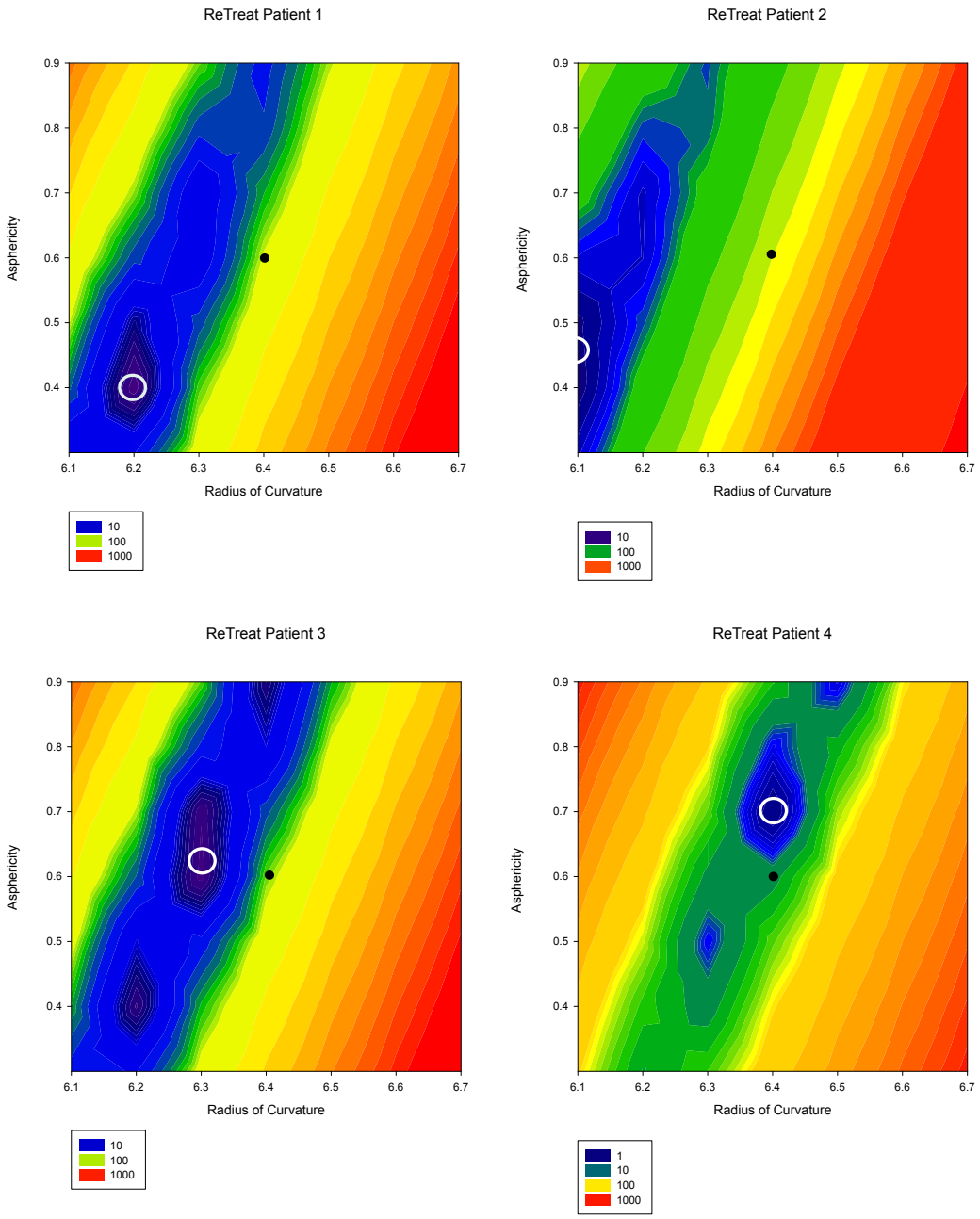

Figure 5.4: Values of RMS error (arbitrary units) shown as the posterior cornea varies over radius of curvature and asphericity for each retreat patient. The black spot represents the parameters where the original data were taken. The best result due to adjustment is shown within the white circle.

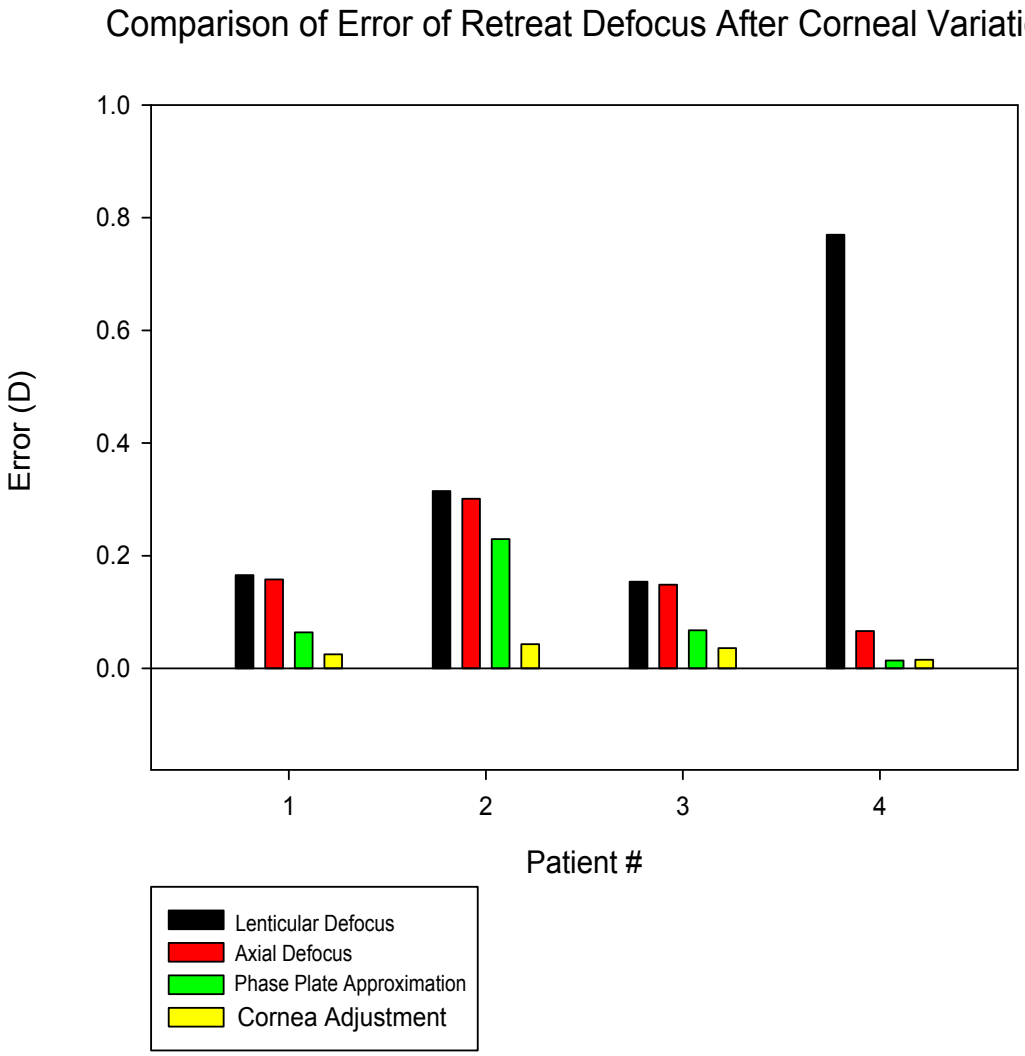

Figure 5.5: A comparison of predicted error of retreat patients' defocus versus error when the cornea is allowed to vary. Yellow bars show the comparison of the new defocus when the posterior cornea is varied slightly to the previous fits for the retreat group.

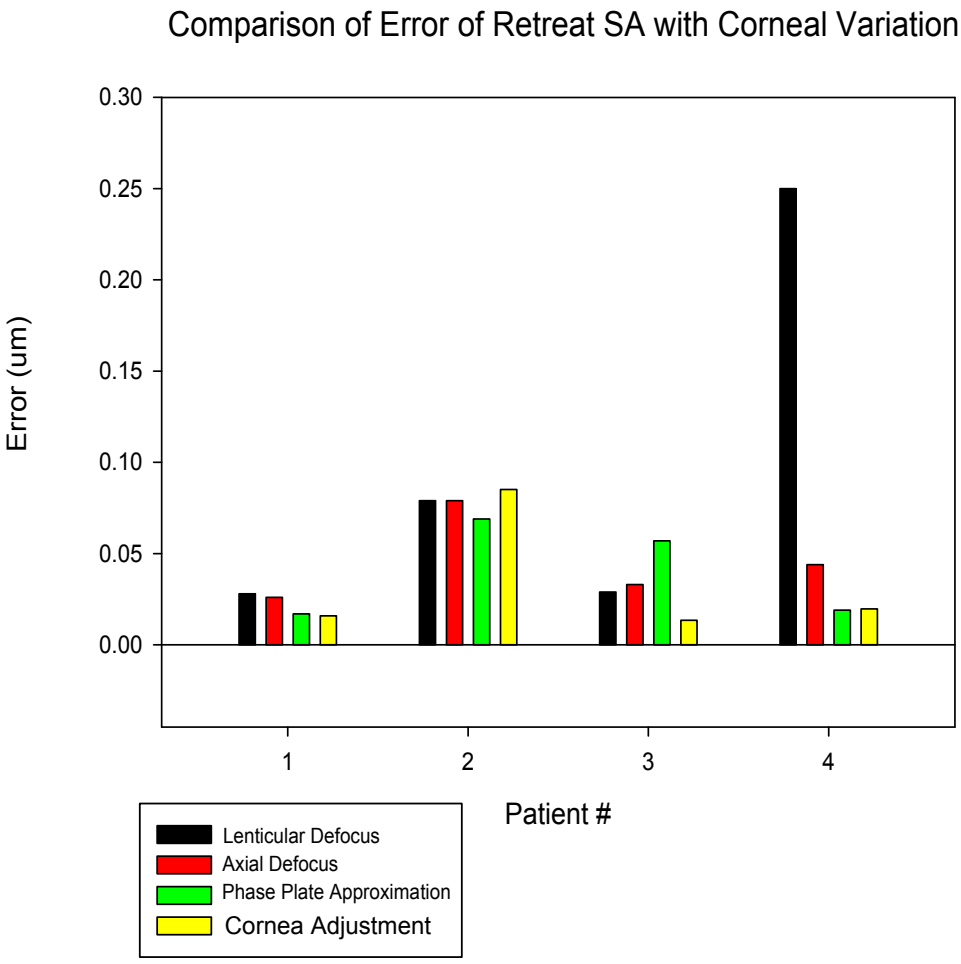

Figure 5.6: A comparison of predicted error of retreat patients' SA versus error when the cornea is allowed to vary. Yellow bars show the comparison of the new spherical aberration when the posterior cornea is varied slightly to the previous fits for the retreat group.

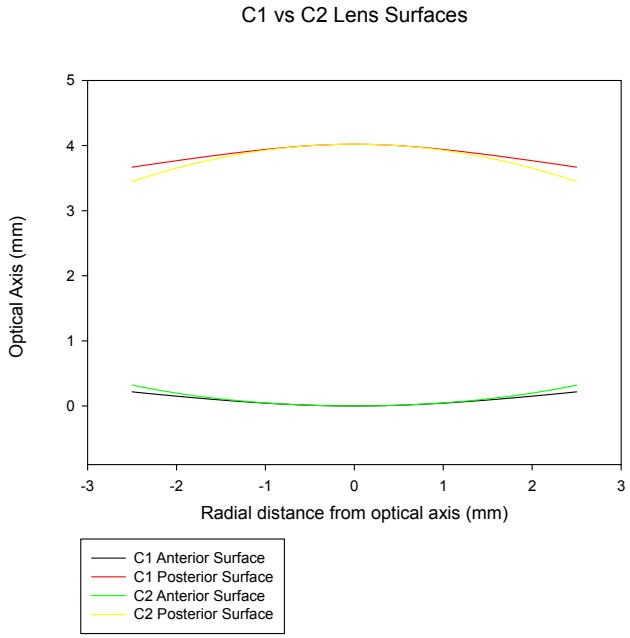

Figure 5.7: The portion of the surface of the lenses of patients G1 and G2 where light is incident.

is patient G1, where it was found that $W = 95.00$, $q_{ant} = -12.91$ and $q_{pos} = -30.82$. None of these values are within the demonstrated range of human eye parameters (Table 1.1). Of these, the W value is shown to be reasonable mostly easily. In Figure 2.4, it can be seen that as W increases beyond 5, the change in index distribution is far less pronounced than it is from even 0.5 to 1. If $W = 95.00$ were added to this plot, it would be barely distinguishable from $W = 10.0$.

Parameters $q_{ant} = -12.91$ and $q_{pos} = -30.82$ are also outside of the normal values for lenticular asphericity. However, light travelling through the eye will never encounter the edge of the lenticular surface due to the pupil. In Figure 5.7, the lenticular surfaces of patient G1 and G2 are plotted over the range that light will actually interact with the lens.

It is immediately clear from this figure that G1's unusual values of asphericity

do not carry a huge weight. This is due to the fact that light is only incident near the apexes of the surfaces (which extend roughly twice the distance shown), and asphericity shows a much greater effect near the edge of the surface.

The computational reason behind these extreme parameters is the end condition on the simplex fitting algorithm (discussed in section 3.5). Both absolute and relative termination conditions were set too tight, causing the algorithm to search for physically unrealistic fit quality. Since patient G1 is the only case with parameters outside of the usual human range, we may conclude that our fit parameters are reasonable. However, for future fits, both constraining the parameters within a normal human range and adjusting fit end conditions will be attempted, as we have shown the sensitivity is low outside of human range.

The biggest limitation to this study is the lack of information available regarding the eye biometry of the patients. Without this data, we were forced to make many assumptions throughout the methodology that would otherwise be unnecessary. Additionally, too many parameters were allowed to float or had to be scanned through in order to find good pre-operation fits. Because of this, there were multiple results that had high correspondence to the target data (of which only the best were shown in this study).

Inherent in this work is the assumption that C_0, C_1 and C_2 can be considered constant in humans. This assumption remains untested after this work, as too many possible sets of lens parameters were available to necessitate their adjustment. If the full biometry of an individual eye is known, and W is the only parameter left to float in a fit, it might prove that this assumption is valid, and that our model is able to fully replicate the optical properties of individual human eyes to a very high accuracy level.

Despite the limitations, the results shown in this work indicate that the model

lens proposed is very successful in replicating the behaviour of the lenses of individual patients. It is highly recommended by the author that a full study be conducted (with complete biometric information on each patient) in order to fully resolve questions surrounding the C_0, C_1 and C_2 parameters in human eyes, as well as to improve the model.

5.4 Conclusions and future work

The following conclusions may be drawn resulting from work presented in this thesis:

1. Our eye model can successfully predict the defocus and spherical aberration of an individual's eye using only anterior corneal surface, the pupil radius, and the optical aberration.

2. The lens predicted in this way is sufficient to predict results from a refractive surgery if the posterior cornea is allowed to vary slightly from its pre-operation surface.

As stated in Chapter 1, the working hypothesis was: A model of the crystalline lens can be constructed which will be able to accurately predict the optical parameters of an individual human eye. This model must be constructed using only aberration information obtainable from common clinical aberrometer readings and biometry information available in-vivo. This study does not have access to a set of full biometric information, and attempts to use only corneal data with no knowledge of the crystalline lens or eye length.

Indeed, a model of the crystalline lens was shown to be able to correctly predict the optical parameters of an individual human eye. This model needed only clinical data regarding the ocular wavefront and anterior corneal topography, meeting the

information requirements of the hypothesis. Clearly, this work demonstrates that the working hypothesis was correct.

The next step for this model would be to undergo a full study with complete biometric information. Such a study would allow for the characterization of the C_0, C_1 and C_2 parameters in humans. Further investigation into additions to the model such as lens offset from the optical axis or lens tilt might be able to offer additional accuracy in matching non-symmetrical Zernike coefficients, and would present further conclusions regarding the applicability of this model in a clinical setting.

References

[1] A.G. Bennett and R.B. Rabbetts. *Clinical Visual Optics, 2nd edition*. Butterworth-Heinemann, 1996.

[2] D.A. Atchison and G. Smith. *Optics of the Human Eye*. Butterworth-Heinemann, 2002.

[3] David Borja, Fabrice Manns, Arthur Ho, Noel Ziebarth, Alexandre M Rosen, Rakhi Jain, Adriana Amelinckx, Esdras Arrieta, Robert C Augusteyn, and Jean-Marie Parel. Optical power of the isolated human crystalline lens. *Investigative ophthalmology & visual science*, 49(6):2541–8, June 2008.

[4] Alberto de Castro, Judith Birkenfeld, Bianca Maceo, Fabrice Manns, Esdras Arrieta, Jean-Marie Parel, and Susana Marcos. Influence of shape and gradient refractive index in the accommodative changes of spherical aberration in non-human primate crystalline lenses. *Investigative ophthalmology & visual science*, 54(9):6197–207, January 2013.

[5] Sanjeev Kasthurirangan, Emma L Markwell, David a Atchison, and James M Pope. In vivo study of changes in refractive index distribution in the human crystalline lens with age and accommodation. *Investigative ophthalmology & visual science*, 49(6):2531–40, June 2008.

[6] P.H. Alsbirk. Variation and Heretability of Ocular Dimensions. *Acta Ophth*, (55):443–456, 1977.

[7] J. Koretz, G. Handelman, and N. Brown. Analysis of human crystalline lens curvature as a function of accommodative state and age. *Vis Res*, (24):1140–1151, 1984.

[8] N Brown. The Change in Shape and Internal Form of the Lens of the Eye on Accommodation. *Experimental Eye Research*, 15:441–459, 1973.

[9] N. Brown. The shape of the lens equator. *Exp. Eye Res.*, (19):571–576, 1974.

[10] M. Bechmann. Central corneal thickness determined with optical coherence tomography in various types of glacucoma. *Br J Ophthalmol*, (84):1233–1237, 2000.

[11] Hwey-Lan Liou and Noel a. Brennan. Anatomically accurate, finite model eye for optical modeling. *Journal of the Optical Society of America A*, 14(8):1684, August 1997.

[12] R. Goyal. Comparison of laser interferometry and ultrasound A-scan in the measurement of axial length. *Acta Ophth*, (81):331–335, 2003.

[13] J. Koretz, C. Cook, and P. Kaufman. Aging of the human lens: changes in lens shape at zero-diopter accommodation. *J. Opt. Soc. Am. A*, (18):265–272, 2001.

[14] B. Moffat, D. Atchison, and J. Pope. Age-related changes in refractive index distribution and power of the human lens as measured by magnetic resonance micro-imaging in vitro. *Vision Res*, (42):1683–1693, 2002.

[15] B. Pierscionek. Refractive Index Contours in the Human Lens. *Exp. Eye. Res.*, (64):887–893, 1997.

[16] D.A. Goss. Ocular Components Measured by Keratometry, Phakometry and Ultrasonography in Emmetropic and Myopic Optometry Students. *Optom. and Vis. Sci.*, (74):489–495, 1997.

[17] Fabrice Manns, Viviana Fernandez, Stanley Zipper, Samith Sandadi, Marie Hamaoui, Arthur Ho, and Jean-Marie Parel. Radius of curvature and asphericity of the anterior and posterior surface of human cadaver crystalline lenses. *Experimental Eye Research*, 78(1):39–51, January 2004.

[18] A. Glasser and M. Campbell. Presbyopia and the Optical Changes in teh Human Crystalline Lens with Age. *Vision Res*, (38):1991–2015, 1998.

[19] Adrian Glasser and Melanie C.W. Campbell. Biometric, optical and physical changes in the isolated human crystalline lens with age in relation to presbyopia. *Vision Research*, 39(11):1991–2015, June 1999.

[20] M. Dunne. Normal Variations of the Posterior Corneal Surface. *Acta Ophth*, (70):255–261, 1992.

[21] J. Francois and F. Goes. Ultrasonographic Study of 100 Emmetropic Eyes. *Ophthalmologica*, (175):321–327, 1977.

[22] Stephen R Uhlhorn, David Borja, Fabrice Manns, and Jean-Marie Parel. Refractive index measurement of the isolated crystalline lens using optical coherence tomography. *Vision research*, 48(27):2732–8, December 2008.

[23] P. Rosales, M. Dubbelman, S. Marcos, and R. van der Heijde. Crystalline lens radii of curvature from Purkinje and Scheimpflug imaging. *Journal of vision*, 6:1057–1067, 2006.

[24] Raksha Urs, Fabrice Manns, Arthur Ho, David Borja, Adriana Amelinckx, Jared Smith, Rakhi Jain, Robert Augusteyn, and Jean-Marie Parel. Shape of the isolated ex-vivo human crystalline lens. *Vision Research*, 49(1):74–83, January 2009.

[25] M. Dubbelman. The Thickness of the Aging Human Lens Obtained from Corrected Scheimpflug Images. *Optom. and Vis. Sci.*, (78):411–416, 2001.

[26] M. Dubbelman and G. van der Heijde. The shape of the aging human lens: curvature, equivalent refractive index and the lens paradox. *Vision Res*, (41):1867–1877, 2001.

[27] M. Howcroft and J. Parker. Aspheric Curvatures for the Human Lens. *Vision Res*, (17):1217–1223, 1977.

[28] J. Koretz, C. Cook, and J. Kuzak. The Zones of Discontinuity in the Human Lens: Development and Distribution with Age. *Vision Res*, (34):2955–2962, 1994.

[29] Wei Wang, Zhao-Qi Wang, Yan Wang, and Tong Zuo. Optical aberrations of the cornea and the crystalline lens. *Optik - International Journal for Light and Electron Optics*, 117(9):399–404, September 2006.

[30] T. Eysteinsson. Central Corneal Thickness, Radius of the Corneal Curvature and Intraocular Pressure in Normal Subjects Using Non-Contact Techniques: Reykjavik Eye Study. *Acta Ophth Scand*, (80):11–15, 2002.

[31] B. Gilmartin. Myopia: precedents for research in the twenty-first century. *Clin. Exp. Ophth.*, (32):305–324, 2004.

[32] George Smith, Michael J Cox, Richard Calver, and Leon F Garner. The spherical aberration of the crystalline lens of the human eye. *Vision Research*, 41(2):235–243, January 2001.

[33] L. Garner and G. Smith. Changes in equivalent and gradient refractive index of the crystalline lens with accommodation. *Optom. Vis Sci.*, (74):114–119, 1997.

[34] Cynthia Wilson. *A Fully Customizable Anatomically Based Model of the Crystalline Lens*. PhD thesis, University of Ottawa, 2010.

[35] MH. Freeman. *Optics, 10th ed.* London, Butterworths, 1999.

[36] L. Thibos, M. Ye, X. Zhang, and A. Bradley. The chromatic eye: a new reduced-eye model of ocular chromatic aberration in humans. *Applied Optics*, 31(19), 1992.

[37] S. Nakao and S. Fujimoto. Model of Refractive-Index Distribution in the Rabbit Crystalline Lens. *Journ. Opt. Soc. Am.*, 8(58):1125–1130, 1969.

[38] S. Nakao, T. Ono, R. Nagata, and S. Iwata. The distribution of refractive indicies in the human crystalline lens. *Jap. J. Clin. Opthal.*, (23):41–44, 1969.

[39] O. Pomerantzeff, H. Fish, J. Govignon, and C. Schepens. Wide-angle optical model of the eye. *Journ. Opt. Soc. Am.*, (19):387–388, 1972.

[40] P. Chu. Nondestructive measurement of index profile of an optical-fibre preform. *Electronics Letters*, 13(24):736–737, 1977.

[41] M. Campbell and A. Hughes. An analytic, gradient index schematic lens and eye for the rat which predicts aberrations for finite pupils. *Vis Res*, (21):1129–1148, 1981.

[42] M. Campbell. Measurement of the refractive index in an intact crystalline lens. *Vis Res*, (24):409–415, 1984.

[43] R. Munger, M. Campbell, and I. Belanic. Refractive index distribution in mammallian lenses: test for elliptical symmetry. *OSA Technical Digest Series, VSIA*, (2):76–79, 1990.

[44] W. Jagger. The Refractive Structure and Optical Properties of teh Isolated Crystalline Lens of the Cat. *Vis. Res.*, (5):723–738, 1990.

[45] G. Smith, D. Pierscionek, and A. Atchison. The optical modeling of the human lens. *Opthal. Phys. Opt.*, (11):357–369, 1991.

[46] Issam H. Al-Ahdali and M. a. El-Messiery. Examination of the effect of the fibrous structure of a lens on the optical characteristics of the human eye: a computer-simulated model. *Applied Optics*, 34(25):5738, September 1995.

[47] Yanqiao Huang and Duncan T. Moore. Human Eye Modeling Using a Single Equation of Gradient Index Crystalline Lens for Relaxed and Accommodated States. In G. Groot Gregory, Joseph M. Howard, and R. John Koshel, editors, *International Optical Design Conference 2006*, volume 6342, page 6342, January 2007.

[48] Rafael Navarro, Fernando Palos, and Luís M González. human lens . II . Optics of the accommodating aging lens. *Journal of the Optical Society of America A*, 24(9):2911–2920, 2007.

[49] Mehdi Bahrami and Alexander V. Goncharov. Geometry-invariant GRIN lens: iso-dispersive contours, 2012.

[50] D. Guang-ming. *Wavefront optics for vision correction.* SPIE, 2008.

[51] Larry N Thibos, Raymond A Applegate, James T Schwiegerling, and Robert Webb. Standards for Reporting the Optical Aberrations of Eyes. 35:232–244, 2000.

[52] Francis Jenkins and Harvey White. *Fundamentals of Optics, 5th Edition.* McGraw-Hill, 1978.

[53] W.T. Welford. *Aberrations of Optical Systems.* Adam Hilger, 1986.

[54] Edmund Optics. Double-convex lens. Catalogue.

[55] William Press. *Numerical Recipes, Third Edition*. Cambridge University Press, 2007.

[56] Erich W. Marchand. Gradient-index imaging optics today. *Applied Optics*, 21(6):983, March 1982.

[57] Anurag Sharma, DV Kumar, and AK Ghatak. Tracing rays through graded-index media: a new method. *Applied Optics*, 21(6):4–7, 1982.

[58] Daniel W Hewak and John W Y Lit. Generalized dispersion properties of a four-layer thin-film waveguide. *Applied optics*, 26(5), 1987.

[59] Lucian Montagnino. Ray Tracing in Inhomogeneous Media. 58(December):1667–8, 1968.

[60] W H Southwell. Index profiles for generalized Luneburg lenses and their use in planar optical waveguides. *Journal of the Optical Society of America*, 67(February):1010–1014, 1977.

[61] J Lit and D Hewak. Numerical ray-tracing methods for gradient index media. *Canadian Journal of Physics*, 63:234, 1984.

[62] R. Luneburg. *Mathematical Theory of Optics.* Brown University, 1964.

[63] Ronald Cubalchini. Modal wave-front estimation from phase derivative measurements. *J Opt. Soc. Am*, 69(7):972–978, 1979.

[64] Pablo Artal, D Ph, Antonio Guirao, D Ph, Esther Berrio, Patricia Piers, Sverker Norrby, and D Ph. Optical Aberrations and the Aging Eye. *International Ophthalmology Clinics*, 43(2):63–77, 2003.

[65] S. Marcos, S. Barbero, L. Llorente, and J. Merayo-Lloves. Optical Response to LASIK Surgery for Myopia from Total and Corneal Aberration Measurements. *Vis Scie*, (42):3349–3356, 2001.